The deeply obscured AGN of NGC 4945

P´erez-Beaupuits, J.P.; Spoon, H.W.W.; Spaans, M.; Smith, J.D.

Published in:
Astronomy & astrophysics

DOI:
10.1051/0004-6361/201117153

Publication date:
2011

A&A 533, A56 (2011)
DOI: 10.1051/0004-6361/201117153

Astronomy & Astrophysics

The deeply obscured AGN of NGC 4945⋆

I. *Spitzer*-IRS maps of [Ne V], [Ne II], H_2 0–0 S(1), S(2), and other tracers

J. P. Pérez-Beaupuits[1,3], H. W. W. Spoon[2], M. Spaans[3], and J. D. Smith[4]

[1] Max-Planck-Institut für Radioastronomie, Auf dem Hügel 69, 53121 Bonn, Germany
e-mail: jp@mpifr.de
[2] Astronomy Department, Cornell University, Ithaca, NY, USA
[3] Kapteyn Astronomical Institute, Rijksuniversiteit Groningen, 9747 AD Groningen, The Netherlands
[4] Department of Physics and Astronomy, Mail Drop 111, University of Toledo, 2801 West Bancroft Street, Toledo, OH 43606, USA

Received 28 April 2011 / Accepted 1 July 2011

ABSTRACT

Context. The nearly edge-on galaxy NGC 4945 is one of the closest galaxies where an AGN and starburst coexist, and is one of the brightest sources at 100 keV. Near and mid-infrared spectroscopy have shown very strong obscuration of its central region, rivaled only in strength by some of the most deeply obscured ULIRGs.
Aims. We determine the spatial distribution of ISM emission features in the central 426 × 426 pc^2 of NGC 4945.
Methods. We mapped the central region of NGC 4945 in three of the four *Spitzer*-IRS modules (SH, SL and LL). In particular, we produced maps of the flux distribution of the starburst tracers [Ne II], [Ne III], [S III] and [S IV] at 12.81, 15.56, 18.71, and 10.51 μm, respectively, and a map of the AGN narrow-line region tracer [Ne V] at 14.32 μm. In addition, we mapped the S(1), S(2), and S(3) pure rotational lines of H_2, which trace the distribution of warm molecular hydrogen. Finally, we obtained an extinction map (A_V) based on the apparent strength of the 9.7 μm silicate absorption feature.
Results. At a spatial resolution of ∼5″, our extinction map traces the contours of the starburst ring. The highest extinction is, however, found at the nucleus, where we measure $A_V(9.85\ \mu m) \approx 60$. Within the uncertainty of the astrometry, all emission lines are found to peak on the nucleus, except for the warm molecular hydrogen emission, which shows a maximum 60–100 pc NW of the nucleus. We favor a scenario in which the emission of the lower H_2 0–0 S(1) and S(2) rotational lines originate mainly in an unobscured extranuclear component associated with the super-wind cone observed in the HST NICMOS map of the H_2 1–0 S(1) vibrational line. For the [Ne V] emission we infer an attenuation of a factor 12–160 (A_V = 55–112) based on a comparison of the ratio of our [Ne V] flux and the absorption-corrected 14–195 keV Swift-BAT flux to the average [Ne V]/BAT ratio for Seyfert 1 nuclei. The high attenuation indicates that [Ne V] and [O IV] cannot be used as extinction-free tracers of AGN power in galaxies with deeply buried nuclei.

Key words. galaxies: active – galaxies: nuclei – galaxies: individual: NGC 4945 – ISM: lines and bands

1. Introduction

At a distance of ∼3.82 Mpc (∼18.5 pc/arcsec, Karachentsev et al. 2007), the active galaxy NGC 4945 is one of the closest galaxies that host both an active galactic nucleus (AGN) and a starburst. Earlier X-ray observations have shown evidence of a hidden AGN (Iwasawa et al. 1993; Guainazzi et al. 2000). These observations revealed a Compton-thick spectrum with an absorbing column density of $N_H = 2.4 \times 10^{24}$ cm^{-2} (Guainazzi et al. 2000). The nucleus of NGC 4945 is one of the brightest extragalactic sources at 100 keV (Done et al. 1996), and the brightest Seyfert 2 AGN at > 20 keV (Itoh et al. 2008).

Rather than a point source marking the presence of the AGN in optical and near-infrared images, the nearly edge-on ($i \sim 80°$) line of sight to the central region reveals strong and patchy extinction, which is especially apparent in HST-NICMOS $H-K$ maps (Marconi et al. 2000). A dust lane aligned along the major axis of the galactic disk obscures parts of the central region just southeast of the K-band peak. The K-band peak itself lies ∼1″ west (but, within the uncertainty) of the position of the H_2O mega maser (Greenhill et al. 1997), which we adopt as the location of the AGN. The mega maser emission allows estimating the mass of the central black hole, $M_{BH} \approx 1.4 \times 10^6\ M_\odot$, which together with its inferred 0.1–200 keV bolometric luminosity of $\sim 2 \times 10^{43}$ erg s^{-1} ($\sim 5 \times 10^9\ L_\odot$, Guainazzi et al. 2000) indicates that the central engine radiates at ∼10% of its Edington luminosity (Greenhill et al. 1997; Madejski et al. 2000).

Estimates from IRAS observations indicate that about 75% of the total infrared luminosity of the galaxy ($L_{IR} = 2.4 \times 10^{10}\ L_\odot$) is generated within an elongated region of 12″ × 9″ (about 222 × 167 pc^2) centered on the nucleus (Brock et al. 1988). The structure of this region, as shown in high-resolution HST-NICMOS observations of the Paα line, is consistent with a nearly edge-on starburst disk with a 4.5″ (∼83 pc) radius (Marconi et al. 2000), embedded in an $r = 8''$ (∼150 pc) inclined (62 degrees) molecular disk (Chou et al. 2007).

Although the star formation and supernova rates in the nuclear region were originally estimated to be moderate

⋆ We dedicate this paper to the memory of our esteemed colleague and advisor, Alan Moorwood (1945–2011), who pioneered the infrared spectroscopic study of NGC 4945. This work is based on observations obtained with the *Spitzer* Space Telescope, which is operated by the Jet Propulsion Laboratory, California Institute of Technology, under NASA contract 1407.

(~0.4 $M_\odot$ yr^{-1} and ~0.05 yr^{-1}, respectively; Moorwood & Oliva 1994), more recent estimates based on high-resolution (angular scale of 0.3 pc) radio observations and estimates of supernova remnant source counts, sizes, and expansion rates, lead to a type II supernova rate of $>0.1(v/10^4)$ yr^{-1} and star formation rate (SFR) limits of $2.4(v/10^4) < SFR(M \geq 5\ M_\odot) < 370\ M_\odot$ yr^{-1}, where v is the shell radial expansion velocity in km s^{-1} (Lenc & Tingay 2009). These supernova and star formation rates are, within a factor of two, similar to those estimated in NGC 253 and M 82 (Pedlar et al. 2003; Lenc & Tingay 2006), which are also nearly edge-on starburst galaxies and which have similar distances close to 4 Mpc, and all show similar infrared luminosities (Rice et al. 1988). The impact of the central starburst on the circumnuclear region is strong, as revealed by the presence of a conical cavity evacuated by a supernova driven wind (Moorwood et al. 1996b; Marconi et al. 2000). The HST-NICMOS images of the H_2 1−0 S(1) line at 2.12 μm show that the edges of the cavity extend out to 5″ (~93 pc) north of the NGC 4945 nucleus (Marconi et al. 2000).

Near and mid-infrared spectroscopy indicate that the ISM line of sight to the central region of NGC 4945 is very different than that of other nearby starburst galaxies, such as M 82 and NGC 253, which present similar inclination angles. The strong absorption features of both volatile (CO and CO_2) and refractory (H_2O) ices observed in the 2.4–5 μm ISO-PHT-S spectrum indicate there are shielded cold molecular clouds obscuring the NGC 4945 nucleus (Spoon et al. 2000, 2003). The detection of a strong absorption feature of XCN ice at 4.62 μm by Spoon et al. (2000, 2003) indicates that these molecular clouds have been processed in an energetic environment (Lacy et al. 1984), and processed ice is said to be a common characteristic of dense molecular material in star-forming galactic nuclei (Spoon et al. 2003). A highly distorted PAH emission spectrum produced by a very deep 9.7 μm silicate absorption feature is more evidence for the unusually strongly obscured nuclear region (Spoon et al. 2000; Brandl et al. 2006). This makes NGC 4945 a unique nearby laboratory to study an environment that can only be found in distant ULIRGs.

Previous mid-infrared spectroscopic observations could not confirm the presence of an AGN in NGC 4945. Just an upper limit of the 14.32 μm [Ne V] emission, considered a tracer of AGN narrow-line regions (e.g., Moorwood et al. 1996a; Genzel et al. 1998), was obtained from ISO-SWS observations (Spoon et al. 2000). The VLT-ISAAC observation of the 3.93 μm [Si IX] line, commonly observed in the soft X-ray photoionized gas of many Seyfert galaxies (Oliva et al. 1994; Lutz et al. 2002), resulted in a non-detection (Spoon et al. 2003). Only recent observations with the more sensitive IRS-SH spectrograph on *Spitzer* allowed detection (although at a very faint level) of the 14.32 μm [Ne V] line towards the NGC 4945 nucleus (Bernard-Salas et al. 2009). The [Ne V]14.3 μm/[Ne II]12.8 μm flux ratio found in NGC 4945 is ~0.007, which indicates an AGN contribution of less than a few percent using the diagram by Farrah et al. (2007, their Fig. 16). This detection of [Ne V] relative to [Ne II] is about ten times weaker than what was observed in other Seyfert galaxies such as Mrk 266 and NGC 1365 (Bernard-Salas et al. 2009).

In this paper we study the mid-IR properties of the nuclear region of NGC 4945. *Spitzer*-IRS spectral mapping observations of a 23″ × 23″ (about 426 × 426 pc^2) region are presented. The mapping capabilities of *Spitzer*-IRS allow the study of a number of properties of the nuclear region in NGC 4945: for instance, the extent of the AGN coronal line region as traced by the [Ne V] line, the extent of the crystalline silicate absorbing region (and a search for the sources responsible for the presence of crystalline silicates), disentangling PAH emission and silicate absorption along the line of sight, and the excitation and age of the circumnuclear-nuclear starburst based on line ratios of forbidden lines. Although we actually used the *Spitzer*-IRS modules SH, SL, and LL in this work, we present the most interesting results only from the SH and SL spectral maps, since we focus on the analysis of the spatial distribution of ISM emission and absorption features. We present for the first time the maps of the starburst tracers [Ne II] 12.81 μm, [Ne III] 15.56 μm, [S III] 18.71 μm, and [S IV] 10.51 μm, and a map of the AGN narrow-line region tracer [Ne V] at 14.32 μm, and analyze the ratios between some of these tracers as different diagnostics. The organization of this article is as follows. In Sect. 2 we describe the observations and the data reduction. The maps obtained are presented in Sect. 3. The analysis of the data is presented in Sect. 4. The conclusions and final remarks are presented in Sect. 5.

2. Observations and data reduction

We mapped the central region of NGC 4945 with the InfraRed Spectrograph[1] (IRS – Houck et al. 2004) on board the *Spitzer* Space Telescope (Werner et al. 2004) through the guaranteed time observation (GTO) program P40018 (PI: H. W. W. Spoon). The spectral maps were done in moderate resolution ($R \sim 600$) with the short-high (SH; 9.9−19.6 μm) IRS[2] module, and at low resolution ($R \sim 60$−120) using the short-low (SL1; 7.4−14.5 μm, SL2; 5.2−7.7 μm) and long-low (LL1; 19.5−38.0 μm, LL2; 14.0−21.3 μm) IRS modules.

The SH module was used to measure mainly the fine-structure emission lines (starburst tracers) [S IV] at 10.51 μm, [Ne II] at 12.81 μm, [Ne III] at 15.56 μm, [S III] at 18.71 μm, the AGN narrow-line region tracer [Ne V] at 14.32 μm, and the molecular hydrogen (pure rotational) lines, H_2 0−0 S(2) and H_2 0−0 S(1) at 12.3 μm and 17.0 μm, respectively. With the SL module we obtained maps of the H_2 S(3), and the silicate absorption feature at 9.7 μm.

2.1. SH map

The IRS-SH map was obtained in July 2007 (at the beginning of the summer visibility window) when the SH slit was relatively aligned with the minor axis of NGC 4945. The area mapped was limited to a set of three parallel by ten perpendicular pointings centered on the nucleus and covering an area of 21″ × 26″. The *top panel* of Fig. 1 shows the orientation of the SH slit overlaid on the *Spitzer*-MIPS 24 μm map of the central region of NGC 4945 (by courtesy of Varoujian Gorjian, priv. comm.).

The quality of the map was optimized by splitting up the mapping into four 1-cycle maps of 120 s, each of which was alternated with a staring mode off-source sky measurement to keep track of rogue pixels and to obtain an accurate measure of the sky background. The total time used for the SH map, including sky positions, was 6.5 h.

[1] The IRS was a collaborative venture between Cornell University and Ball Aerospace Corporation funded by NASA through the Jet Propulsion Laboratory and the Ames Research Center.

[2] http://ssc.spitzer.caltech.edu/irs/highleveloverview

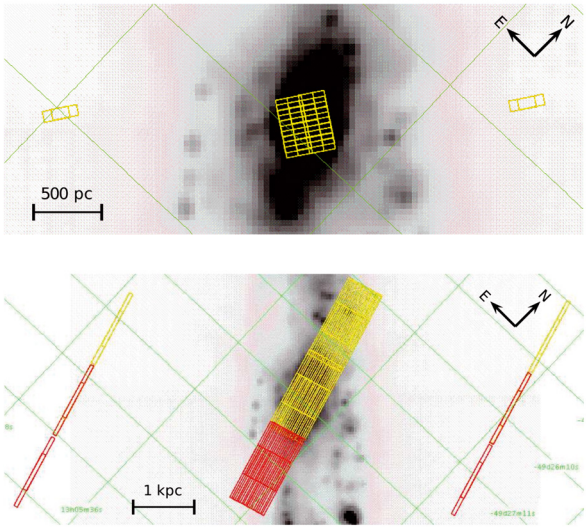

Fig. 1. *Spitzer*-MIPS 24 μm map (Varoujian Gorjian, priv. comm.) of the central region of NGC 4945. The galaxy major axis runs vertical. North is toward the upper right, east toward the upper left. Along the declination axis, the grid spacing is ~1 arcmin, and about 12 s along the RA axis. The region mapped with the IRS-SH module (*top panel*) is about 21″ × 26″, while a larger region of 37″ × 67″ was mapped with the IRS-SL (*bottom panel*) module. The red and yellow grids correspond to the SL1 and SL2 spectral orders, respectively. The sky (off-source) positions observations are indicated by the grids to the left and right of the galaxy major axis. The images were produced with the *Spitzer*/Leopard software package used to query the archive and download the data.

2.2. SL map

Due to a *Spitzer anomaly*[3] that began a few hours before the original schedule of the observations, the IRS-SL map of the nuclear region of NGC 4945 was delayed until August 2008, when the SL slit was no longer perfectly aligned with the galaxy major axis. The observations were done with five cycles of 14 s ramps, which allowed mapping a region of about 37″ × 67″ in two sets (shifted along the slit direction) of nineteen pointings parallel to the SL slit and centered on the nucleus of NGC 4945.

To sample the background continuum and to identify rogue pixels, we also obtained off-source spectra with the same integration times and number of cycles at two positions sufficiently above and below the galaxy disk. The off-source spectra were taken before and after the SL mapping. The total time used for the SL map, including sky positions, amounts to 3.1 h. The orientation of the SL slit, overlaid on the *Spitzer*-MIPS 24 μm map of NGC 4945, is shown in the *bottom panel* of Fig. 1.

2.3. Data reduction

The basic calibrated data (BCD) were pre-processed with the *Spitzer* pipeline versions S16.1 for SH and S18.1 for SL. Rogue pixels were cleaned and maps built using the IRS mapping reduction package CUBISM[4], designed by the SINGS[5] legacy team (Smith et al. 2007). With this tool we performed the flux calibration and background subtraction, and estimated the statistical uncertainty at each spectral wavelength. We created the first spectral cubes from the slit observations combined with CUBISM. After creating the first cubes, we further cleaned the data using the back-tracking procedure described in Smith et al. (2007). All the pixels with flux uncertainty larger than 50% were flagged, so they were not used in subsequent reconstructions of the spectral cubes. We iterated on the cleaning procedure by performing visual inspections throughout the maps, of small sections of the spectra around the emission lines, PAH, and silicate features of interest, and we reconstructed the cubes after cleaning new pixels.

The spectral cubes obtained with CUBISM are in units of surface brightness, MJy sr^{-1}, but we converted them to W cm^{-2} μm^{-1} sr^{-1} to work and present the spectra. We used the units of surface brightness W cm^{-2} sr^{-1} to present the maps and flux density W cm^{-2} for the integrated total fluxes. For this we used the conversion 1 arcsec^2 = 2.3504×10^{-11} steradian, knowing that the pixel size[6] of the IRS/SH map is ~2.26 arcsecs/pixel, which leads to 1.2005×10^{-10} steradians that we needed to multiply by in order to get the maps in units of flux density. In the case of IRS/SL the pixel size is ~1.85 arcsecs/pixel, so we have slightly smaller 8.04424×10^{-11} steradians per pixel than in the SH map.

3. Analysis and results

During the data reduction and spectral analysis process, we found that the SH spectral orders[7] are mismatched at levels that vary across the mapped region. This effect is smoothed (although not completely solved) by increasing the overlap between the orders (in the wavsamp calibration file) and by increasing the size of the aperture used to extract 1D average spectra, as discussed below. We also observed module to module mismatches, which inhibit us from reliably combining the SH and SL modules to perform further analyses such as using the H_2 S(3) line as an extinction indicator. These mismatches in the SH orders and between modules have not been addressed before[8], probably because they are only apparent in high S/N data as in those presented in this work. The IRS-SH/SL orders/modules mismatch problem seen in high S/N data is a new issue that we are still studying with members of the SINGS team. Fortunately, most of the emission and absorption features we are interested in are found within the spectral orders, and those features observed near the edge of the orders are treated with extreme care or not addressed at all.

The average spectrum, considering the whole field of view (FOV) of the IRS/SH map, and the average spectrum of the IRS/SL map (extracted from a similar FOV to the one in the SH map) are shown in the *top* and *bottom* panels of Fig. 2, respectively. The most important fine-structure emission lines and PAH features are indicated in both spectra.

We developed our own IDL procedures to work on the 1D spectra that were used to build the final maps. These 1D spectra were extracted from the clean SH cubes by averaging the spectra over a moving 2 × 2 pixel aperture. The whole field of view was covered with a step size of 1 pixel, so the reduced map contains only 10 × 10 pixels of ~2.3″ each (where 1″ corresponds to ≈18.5 pc at the distance of 3.82 Mpc), but covering the same

[3] http://www.spitzer.caltech.edu/news/856-feature06-25-Engineers-Studying-Spitzer-Anomaly
[4] http://ssc.spitzer.caltech.edu/dataanalysistools/tools/cubism/
[5] http://ssc.spitzer.caltech.edu/spitzermission/observingprograms/legacy/
[6] See http://coolwiki.ipac.caltech.edu/index.php/Units for a description of *Spitzer* units and conversions.
[7] http://ssc.spitzer.caltech.edu/irs/irsinstrumenthandbook/
[8] http://ssc.spitzer.caltech.edu/irs/features/

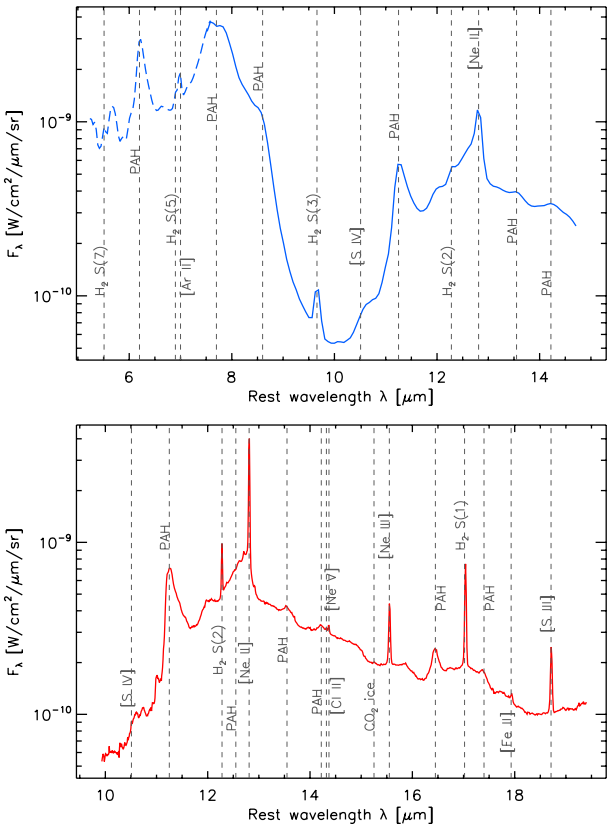

Fig. 2. *Top panel* – Average spectrum of the equivalent field of view of the SH map of the nuclear region of NGC 4945, as seen in the SL map. The SL2 order is shown with a *dashed* line. The most significant fine structure emission lines and PAH features in the SL wave range are labeled, in particular the ones that overlap with the SH waverange. *Bottom panel* – Average spectrum of the whole field of view of the SH map. The higher spectral resolution of the IRS/SH module allows emission lines to be distinguished such as [Ne V]14.32 μm and [Cl II]14.37 μm, otherwise blended in the IRS/SL module. These spectra are not corrected for extinction.

area as the original map. However, the last slit observation of the IRS/SH map covers just about one third of the spatial region associated with each pixel. Therefore, we conclude that the last column of the original 11×11 grid map produced by CUBISM is not representative of the actual spatial region associated with that slit column, and we do not use it in our maps, so the final maps reduced with the 2×2 aperture results in 9×9 pixel maps, covering a slightly smaller region than the original maps. The coordinates assigned to each pixel of the resulting map are those of the center of the 2×2 aperture, and the pixel fluxes reported in Figs. 5, 6, 10, and 11 are the average fluxes in the 2×2 apertures. With the 2×2 pixel extraction box, the S/N of the spectra is increased by a factor 2 (from the $\sqrt{4}$ pixels), and it reduces the effect of the mismatch between orders mentioned above. This corresponds to a standard procedure recommended to obtain IRS maps of extended sources.

The average full width half maximum (*FWHM*) of the IRS/SH point spread function (PSF) has been estimated to be ~5.16″ and ~4.31″ for the direction along the spectral dispersion axis and the spatial axis of the slit, respectively, while the corresponding average PSF *FWHM* values of the SL2 (mostly used in this work) are ~3.76″ and 3.27″, respectively (Pereira-Santaella et al. 2010, their appendix A). The 1-σ deviation around the average centroid position in SL modules was found to be ~20 times smaller than the SL pixel size (1.85″). While the maximum 1-σ deviation in the SH module was found to be ~0.6″, which is considered small compared to the SH pixel size (2.26″).

With the aim of determining whether our line emission maps are resolved, we retrieved a partial map of 3×3 SH slit pointings of the star P Cygni (AOR 13049088). The map consists of 5″ steps parallel to the slit and 2″ steps perpendicular to the slit, similar to the map spacing we have for NGC 4945. These pointings lead to a 10×3 pixel map. To test the continuum drop off along the (10 pixels) slit, 2×2 aperture spectra were extracted in the same way as we do for the SH maps of NGC 4945. Then the continuum flux at 15 μm was measured in each position, resulting in a mostly Gaussian variation of the flux along the slit. The *FWHM* ranges from 6 to 7 arcsec between 10 and 19 microns, far less than the ratio 19/10 expected over this range for the PSF of a diffraction limited telescope. The same procedure was applied to the 12×6 map of the star KsiDra used by Pereira-Santaella et al. (2010) (AORs 16294912 and 16340224). In this case, an *FWHM* in the range 5.8″−6.4″ was found in both the parallel and the perpendicular (to the slit) directions.

From the SH 2×2 aperture average spectra, we obtained maps of the starburst tracers [S IV] at 10.51 μm, [Ne II] at 12.81 μm, [Cl II] at 14.37 μm, [Ne III] at 15.56 μm, [S III] at 18.71 μm, as well as the AGN tracer [Ne V] at 14.32 μm and the pure rotational molecular hydrogen lines, H_2 S(2) and H_2 S(1) at 12.3 μm and 17.0 μm, respectively. For each line we first estimate a continuum level by fitting a second-order polynomial to the base of the emission line or a cubic spline with selected anchor points (pivots) when the emission line was on top of a complex PAH or silicate feature. We applied the same aperture reduction procedure for the SL map, from which we obtained a map of the silicate absorption feature at 9.7 μm and the corresponding silicate strength as described in Sect. 3.4. We also obtained a map of the the molecular hydrogen line H_2 S(3) at 9.66 μm.

3.1. The spectral complex around [Ne V] 14.32 μm

The complexity of the spectral range around the [Ne V] 14.32 μm is shown in Fig. 3. An unknown feature at ~13.95 μm seems to be present just next to the first bending mode of HCN at 14.02 μm. Depending on the temperature of the surrounding molecular gas, HCN can be vibrationally excited by absorbing the infrared photons at 14.0 μm. This will produce a subsequent cascade process that can enhance HCN rotational lines in the (sub-)millimeter range. This corresponds to the IR-pumping scenario proposed to explain the bright HCN $J = 1 \rightarrow 0$ (and higher) transition observed in some ULIRGs and Galactic star-forming regions (e.g., Aalto et al. 1995; García-Burillo et al. 2006; Guélin et al. 2007; Aalto et al. 2007; Pérez-Beaupuits et al. 2010). The mismatch between orders (mentioned in Sect. 3) observed between ~13.90 μm and ~14 μm, also seen by Pereira-Santaella et al. (2010) meant we are unable to conclude whether we actually did detect the HCN 14.02 μm feature, whether in emission or in absorption.

A larger PAH feature is observed around ~14.22 μm, and the fine-structure emission lines of [Ne V] 14.32 μm and [Cl II] 14.37 μm are found on its rightmost (and less steep) slope. Chlorine, which has an ionization potential of 12.97 eV, is known to play an important role in characterizing the neutral gas components in the ISM. When H_2 is abundant (optically thick in the FUV), it reacts (exothermically by 0.17 eV) with [Cl II] to form HCl^+, which leads to the formation of [Cl I] and H I

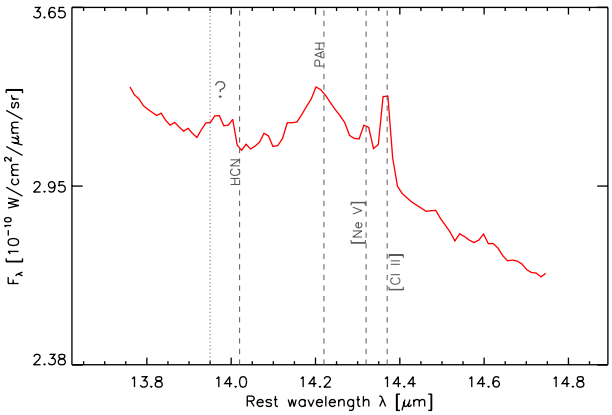

Fig. 3. Zoom into the [Ne V] complex wavelength range from the average IRS/SH spectrum of Fig. 2. At these wavelengths we find the first bending mode of HCN at 14.02 μm, and the AGN tracer [Ne V] at 14.22 μm, almost blended with the fine-structure emission line [Cl II] at 14.37 μm, on the slope of the PAH feature around 14.22 μm. The dotted line shows the wavelength at which we found an order mismatch, probably producing the unknown feature observed next to the HCN 14.02 μm, which could be affected.

(Jura 1974; Jura & York 1978). This means that chlorine is predominantly ionized in H I regions, while it is predominantly neutral when cold H_2 components are present (Sonnentrucker et al. 2002, 2003). The [Cl II] 14.37 μm fine-structure emission line was clearly detected (>3σ) in the whole region mapped with the IRS/SH module, and it presents a similar (although more spread-out) distribution to the [Ne II] 12.81 μm line.

Because its ionization potential (97.1 eV) is too much to allow production by main-sequence stars, the fine-structure line [Ne V] 14.32 μm is commonly used to probe the narrow line region of AGNs (e.g., Moorwood et al. 1996a; Genzel et al. 1998; Sturm et al. 2002; Armus et al. 2007; Alonso-Herrero et al. 2009; Baum et al. 2010; Willett et al. 2010, and references therein). It has recently been used as a diagnostic tool for unambiguously identifying AGN in galaxies that have not been identified as such using optical spectroscopy (Goulding & Alexander 2009).

3.2. Estimating the line emission flux

The emission fluxes were estimated by fitting a Gaussian profile to the fine-structure lines and integrating the flux above a local continuum, which was estimated from a cubic spline interpolation of selected anchor points (pivots). Since we want to determine the actual spatial distribution of the emission lines in the nuclear region of NGC 4945, we set a strict 3σ level detection for all the fine-structure emission lines, and at least two data points (or a full width of ~560 km s^{-1} at 14.32 μm) in the profile, to consider a feature as a real emission line in the spectrum. For a robust estimate of the local continuum, we adopted an average flux of five points around each of the selected pivots used in the cubic spline interpolation. Figure 4 shows the Gaussian fit of the [Ne V] 14.32 μm and [Cl II] 14.37 μm fine-structure emission lines at three different positions of the IRS/SH map. The uncertainty of each spectral data point is indicated by the error bars. The pivots used for the cubic spline interpolation of the local continuum (baseline) are at the 14.201 μm, 14.247 μm, 14.281 μm, 14.428 μm, 14.531 μm, 14.667 μm, and 14.780 μm wavelengths.

The *top panel* of Fig. 4 shows the spectrum in a region of the map with relatively high uncertainties (~1.4% on average) in

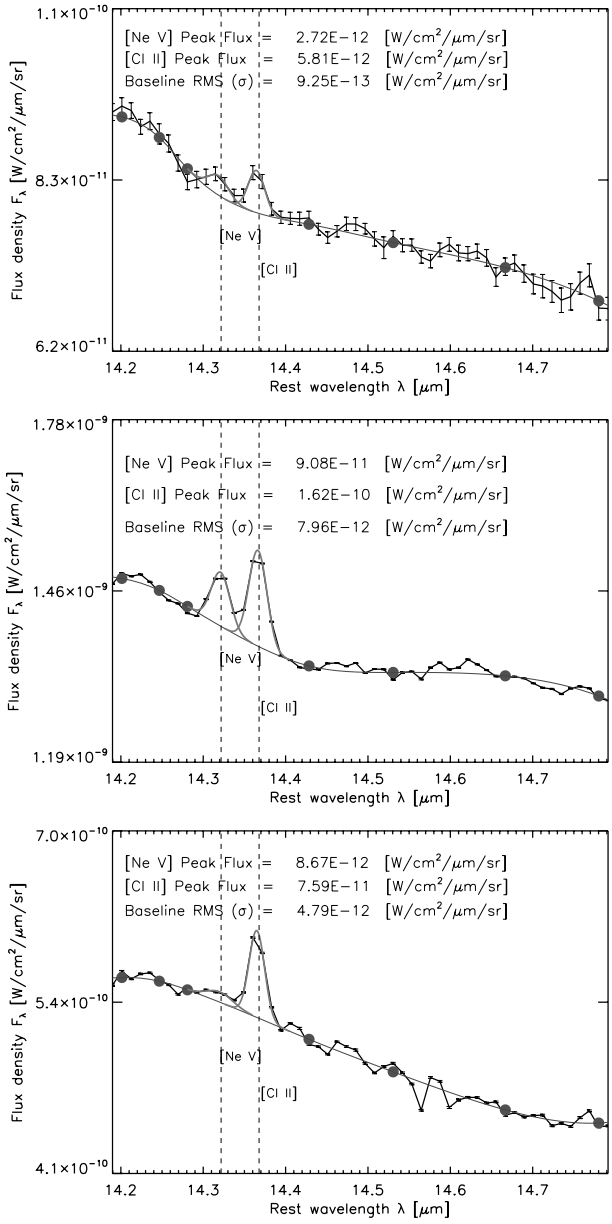

Fig. 4. Gaussian fit of the [Ne V] 14.32 μm and [Cl II] 14.37 μm fine-structure emission lines at three different pixels of the IRS/SH map. The error bars indicate the uncertainties of the spectral data. The filled circles indicates the pivots used for the cubic spline interpolation of the baseline. The *top panel* shows less than 3σ detection for [Ne V] but a clear detection of the [Cl II] line. The spectrum of the *middle panel* shows clear detections of both lines. The *bottom panel* shows <3σ detection for [Ne V], in spite of the low uncertainties in the data points.

the spectral data and with high rms (as computed from the baseline and indicated in the legend of the plots) that leads to less than a 3σ detection for [Ne V], but a clear detection (>3σ) for the [Cl II] line. The spectrum of the *middle panel* was extracted from the central 2×2 pixel aperture of the map, which has an $S/N \sim 9$ in the line and >100 in the continuum, and is among the highest S/N in the whole IRS/SH map. This spectrum shows very low uncertainties (~0.06% on average) in the data and clear detections of both lines. Although with low uncertainties in the data (~0.13%), the *bottom panel* of Fig. 4 shows less than a 3σ detection for [Ne V] (with an $S/N \sim 1.8$), but a strong detection of [Cl II] 14.37 μm. With this Gaussian fit procedure, we

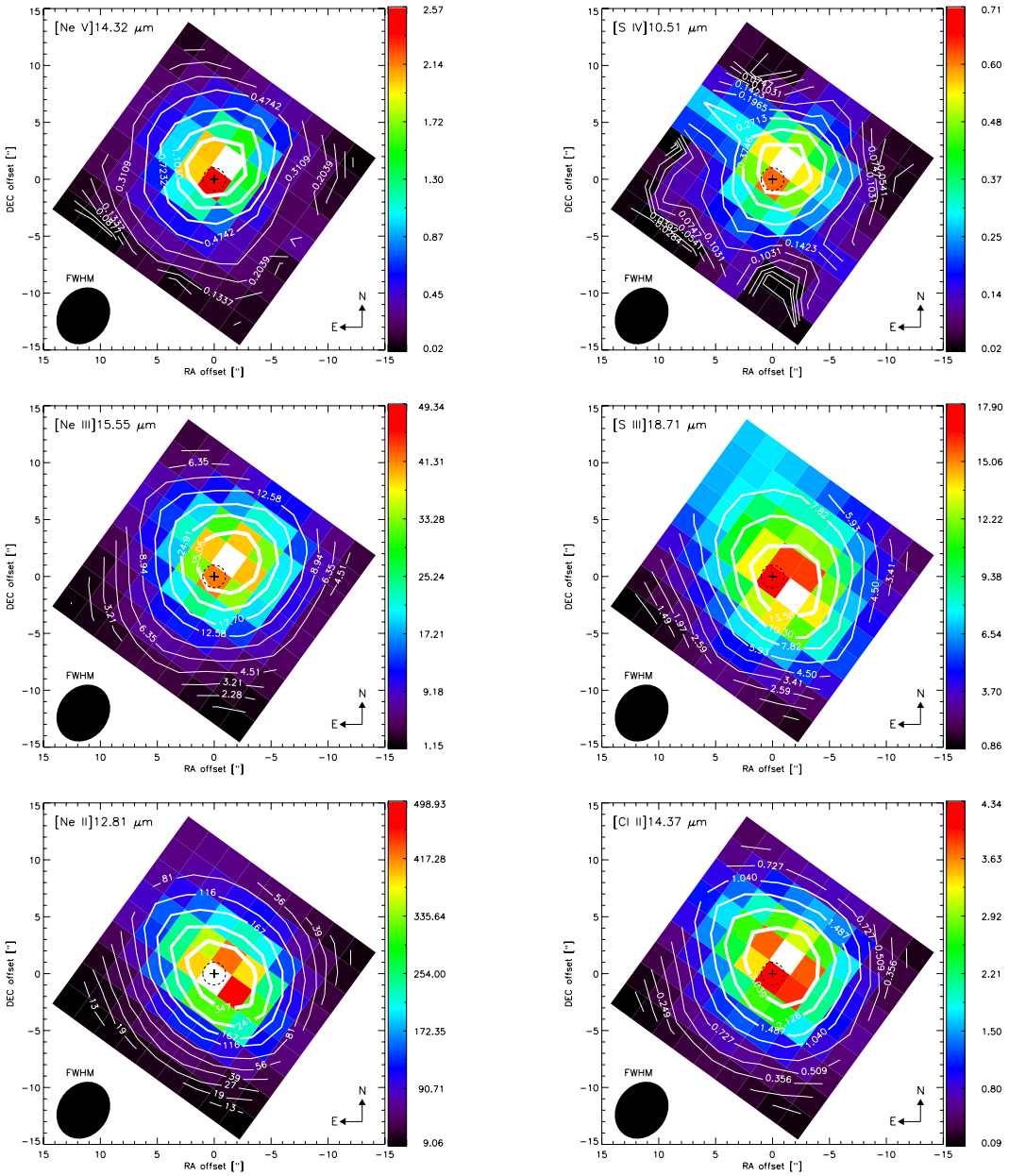

Fig. 5. IRS/SH surface brightness (10^{-12} W cm^{-2} sr^{-1}) maps of the fine-structure lines (*left panels*, from top to bottom) [Ne V] 14.32 μm, [Ne III] 15.55 μm, [Ne II] 12.81 μm, (*right panels*, from top to bottom) [S IV] 10.51 μm, [S III] 18.71 μm, and [Cl II] 14.37 μm. The peak fluxes are shown with a white pixel. These fluxes are not corrected for extinction, and each of the 9×9 pixels correspond to the fitted flux in the 2×2 aperture extracted spectrum as described in Sects. 2.3 and 3.2. The dashed-line circle represents the $\pm 1''$ pointing accuracy of *Spitzer*, and the contour lines are labeled. The reference ($\Delta\alpha = 0, \Delta\delta = 0$) is marked with a cross and corresponds to the position RA (J2000) = 13:05:27.477, Dec (J2000) = –49:28:05.57 of the H_2O mega maser reported by Greenhill et al. (1997).

produced 9×9 pixels maps (as described above) of several fine-structure lines, PAH features, and the silicate absorption feature at 9.7 μm (discussed in Sect. 3.4), covering a region of about $23'' \times 23''$ (about 426×426 pc^2). The SH maps are shown in Figs. 5 and 6. In the case of the [Ne V] 14.32 μm, the pixels with surface brightness lower than 0.1×10^{-12} W cm^{-2} sr^{-1} correspond to a detection level $<3\sigma$.

For the particular case of the [Ne V] line, a Gaussian fit of the uncorrected for extinction map indicates that this emission is only marginally resolved along the major axis, given its *FWHM* of 6.4″. Along the minor axis the *FWHM* is 7.3″. After extinction correction (discussed in Sects. 3.3 and 3.4), the [Ne V] emission appears unresolved. The other emission lines (uncorrected for extinction) are well resolved (*FWHM* > 7″).

3.3. Visual extinction

Lower limits on the reddening in the nuclear region of NGC 4945 were obtained from the HST-NICMOS $H - K$ color image (Marconi et al. 2000). An average color $H - K = 1.1$, yielding an $A_V \approx 11$ mag, was observed in the region of the Paα ring. This A_V is comparable with extinctions over 13 mag, as estimated from the Brα/Brβ and Paα/Hα ratios (Moorwood & Oliva 1988; Marconi et al. 2000).

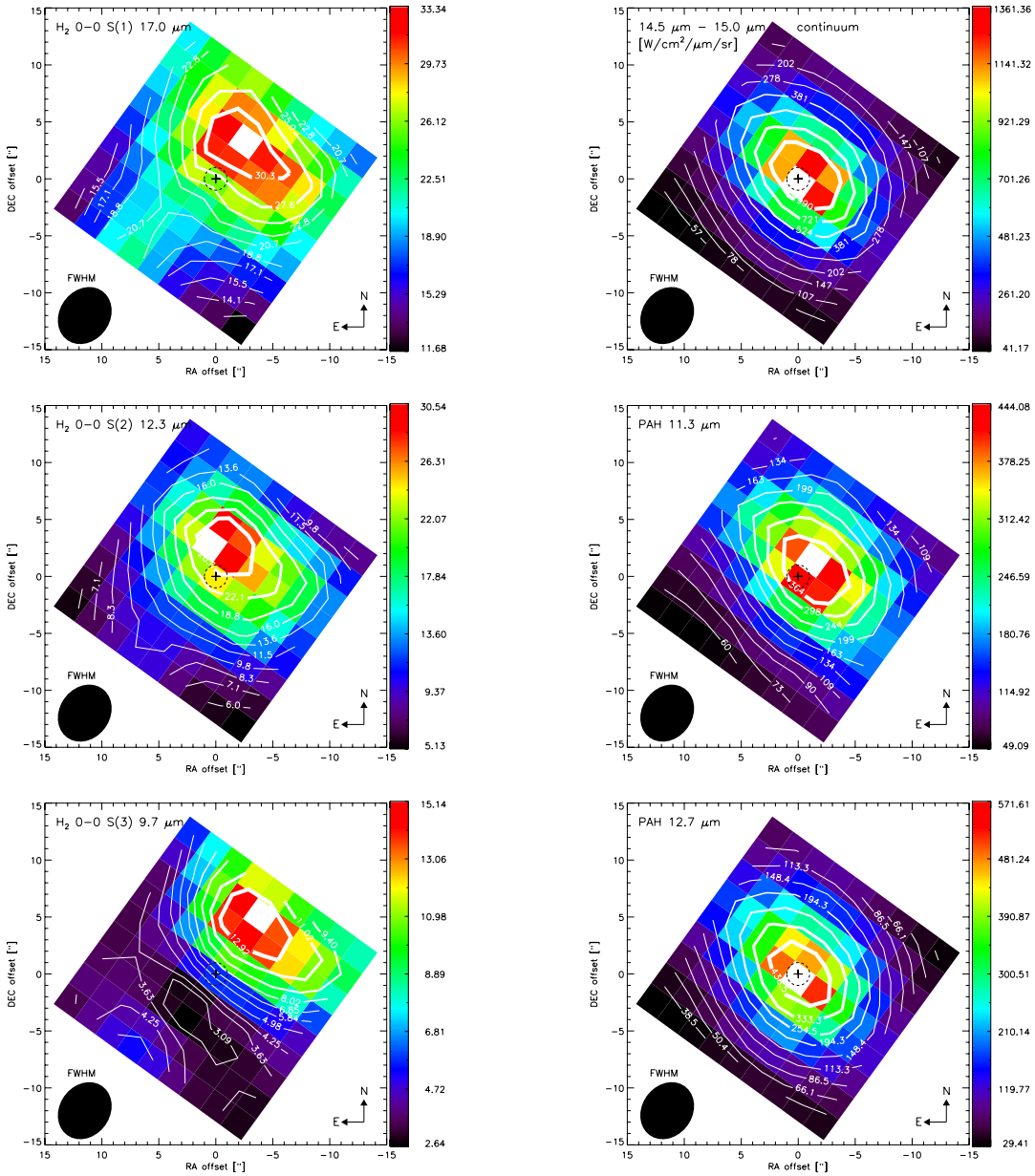

Fig. 6. IRS/SH surface brightness (10^{-12} W cm^{-2} sr^{-1}) maps of the molecular hydrogen lines (*left panels*, from top to bottom) H_2 S(1) at 17.0 μm and H_2 S(2) at 12.3 μm, and the H_2 S(3) line at 9.7 μm from the IRS/SL map. The *right panel* shows (from top to bottom) the average continuum flux density (10^{-12} W cm^{-2} μm^{-1} sr^{-1}) between 14.5 μm and 15.0 μm, and the surface brightness (10^{-12} W cm^{-2} sr^{-1}) of the PAH features at 11.3 μm and 12.7 μm. The details in the maps are the same as in Fig. 5.

To compare this with our data, we produced an image of A_V at the same resolution of the IRS/SH maps, using the HST-NICMOS $H-K$ color image. First, we used the same definition of foreground screen extinction given in Marconi et al. (2000)

$$A_V(H-K) = \frac{E(H-K)}{c(H)-c(K)}, \quad (1)$$

where $E(H-K)$ is the color excess that can be obtained from the difference between the observed and intrinsic colors, $E(H-K) = (H-K) - (H-K)_0$. We used the average intrinsic color $(H-K)_0 \approx 0.22 \pm 0.1$ mag of spiral and elliptical galaxies reported by Hunt et al. (1997). The $c(H)$ and $c(K)$ coefficients are derived from the extinction law, $A_\lambda = c(\lambda)A_V$. But instead of using the $A_\lambda \propto (\lambda/1\ \mu\mathrm{m})^{-1.75}$ law ($\lambda > 1\ \mu$m) assumed by Marconi et al. (2000), we used the extinction law for the local ISM reported by Chiar & Tielens (2006), which considers solid and porous spheres and a continuous distribution of ellipsoids in the extinction profiles used for the amorphous silicates in the 9.7 μm absorption feature. We interpolated the c coefficients at $\lambda = 1.606\ \mu$m and $\lambda = 2.218\ \mu$m of the HST-NICMOS H and K bands, respectively. In Chiar & Tielens (2006) the local ISM continuum extinction was found to be described by the expression

$$\log(A_\lambda/A_K) = 0.65 - 2.4\log(\lambda) + 1.34\log(\lambda)^2, \quad (2)$$

using $A_K/A_V = 0.09$ to normalize the extinction to the K band (Whittet 2003). Beyond 8 μm the silicate profile of WR-98A is superimposed using $A_V/\tau(9.7\,\mu\mathrm{m}) = 18$ (Roche & Aitken 1984). So we used Eq. (2) and $A_K/A_V = 0.09$ to estimate the $c(H)$ and $c(K)$ coefficients for the stellar light-based extinction $A_V(H-K)$.

The *top panel* of Fig. 7 shows the HST-NICMOS $H-K$ mag image reported by Marconi et al. (2000) with the *Spitzer*-IRS

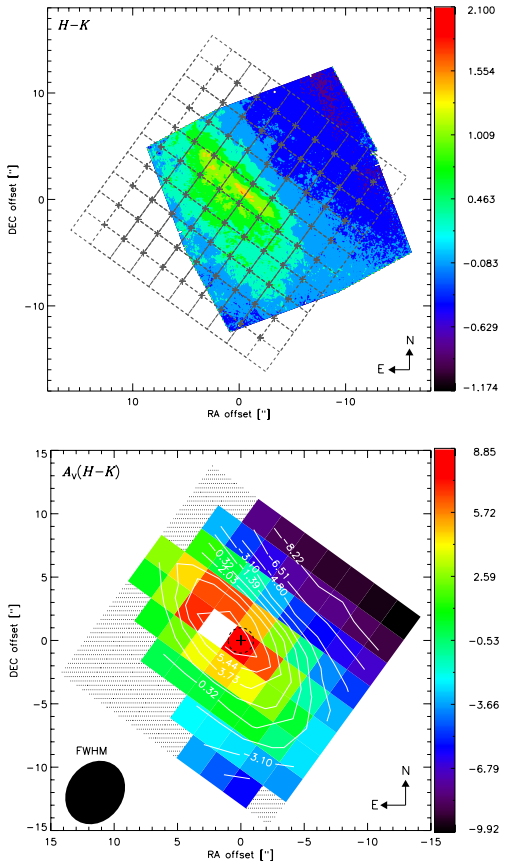

Fig. 7. *Top panel* – HST-NICMOS $H-K$ color image (mag) reported by Marconi et al. (2000). The *Spitzer*-IRS SH grid is overlaid to show the difference in resolution and the different orientations of the fields of view. *Bottom panel* – Foreground screen extinction $A_V(H-K)$ estimated from the $H-K$ color image at the resolution of the IRS/SH map. The SH pixels that cover less than 400 pixels in the $H-K$ image are shown in dashed lines.

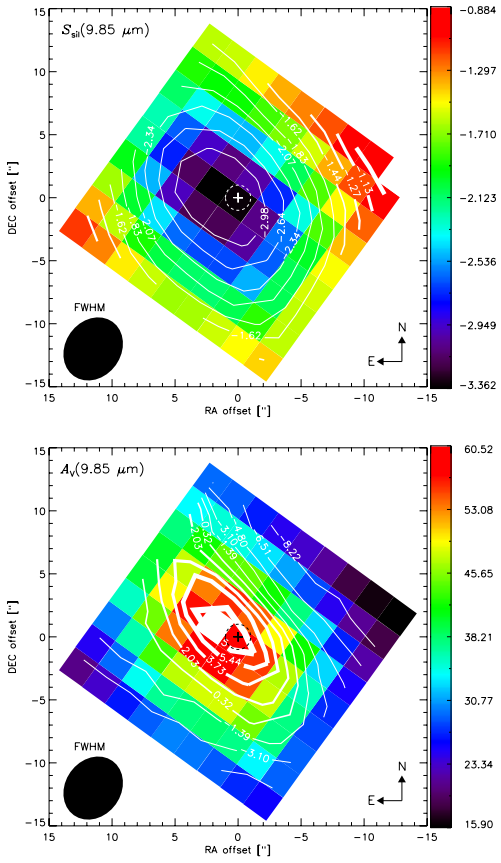

Fig. 8. *Top panel* – IRS/SL map of the apparent silicate strength S_{sil} estimated at 9.85 μm. *Bottom panel* – Silicate-based extinction $A_V(9.85\,\mu m)$ map estimated from the average visual extinction to silicate optical depth ratio $A_V/\tau(9.7\,\mu m) = 18$ for the local ISM (Roche & Aitken 1984; Rieke & Lebofsky 1985) and assuming $\tau(9.7\,\mu m) \approx S_{sil}(9.85\,\mu m)$. The contour lines of the stellar light-based extinction $A_V(H-K)$ of Fig. 7 are overlaid on the $A_V(9.85\,\mu m)$ map (color pixels).

SH grid overlaid. We took all the pixels of the $H-K$ image (which have higher resolution than our maps) that fall within a 2×2 pixel aperture of the SH grid map, and computed the average A_V for that particular pixel. After doing this for every single pixel in the SH grid, we obtained the foreground extinction (at the resolution of the SH map) shown in the *bottom panel* of Fig. 7. Only SH pixels covering more than 400 pixels in the $H-K$ image are considered in our analysis. The peak of this stellar light-derived extinction lies about 2.3″ (one pixel) northeast of the H_2O mega maser.

3.4. The deep silicate absorption around 9.7 μm

From the IRS/SL cubes we can study the amorphous silicate grains, which present a broad and deep absorption feature around 9.7 μm. The presence of PAH emission along the same line of sight as the silicate absorption makes it hard to measure the apparent silicate depth. If one assumes the PAH emission to be foreground to the silicate absorption, then a different apparent silicate depth is found than when it is assumed that they are mixed. Silicate absorption can also be foreground to the PAH emission. Here we use the method proposed by Spoon et al. (2007, their Fig. 2) for absorption-dominated spectra to infer the apparent strength of this silicate feature. First, we extracted a 1D spectra from the SL map rebinned to the 2×2 pixel aperture of the SH map described in Sect. 3. For each spectrum, we adopted a local mid-infrared continuum by interpolating the feature-free continuum pivots at 5.3 μm and 13.55 μm.

Because the S/N is not uniform for all the pixels of the SL map, and the features around 5.3 μm change depending on the proximity to the nucleus of NGC 4945, we used a similar procedure to the one for [Ne V] 14.32 μm (Sect. 3.1). The flux assigned to the pivot at 5.3 μm was adopted as the minimum flux observed between 5.1 μm and 5.5 μm. To avoid contamination from the H_2 S(3) 9.66 μm molecular line, the flux estimated for the deepest point adopted at 9.85 μm was the median flux between 9.7 μm and 10.0 μm. The flux estimated for the pivot at 13.55 μm was the median flux observed between 12.9 μm and 14.0 μm. Then we computed the ratio between the observed flux (f_{obs}) and the estimated continuum flux (f_{cont}) at 9.85 μm, and we obtained the silicate strength S_{sil} as

$$S_{sil} = \ln\left[\frac{f_{obs}(9.85\,\mu m)}{f_{cont}(9.85\,\mu m)}\right]. \quad (3)$$

For sources with a silicate absorption feature, S_{sil} can be interpreted as the negative of the apparent silicate optical depth ($\tau_{9.7\,\mu m}$). The *top panel* of Fig. 8 shows the IRS/SL map (rebinned to the 2×2 aperture of the IRS/SH map) of the apparent silicate strength at 9.85 μm. The silicate-based extinction $A_V(9.85\,\mu m)$, shown in the *bottom panel* of Fig. 8, was estimated from the average visual extinction to silicate optical

depth ratio $A_V/\tau(9.7\ \mu m) = 18$, which is appropriate for the local ISM (Roche & Aitken 1984; Rieke & Lebofsky 1985). The spatial distribution of the silicate-based extinction is similar to that of the stellar light-based extinction $A_V(H-K)$ estimated in Sect. 3.3. The peak extinction is found at the same relative position (ΔRA $\approx 2''$, ΔDec $\approx 1''$), at about $2.3''$ (one pixel) northeast of the H_2O mega maser (Greenhill et al. 1997).

It is known that extinction estimated from optical or near-infrared observations generally underestimates the actual extinction if the environment probed is optically thick at the emission lines observed. If most of the emitting region is obscured, as in the case of the nucleus of NGC 4945, the visual extinction estimate is representative of the surface of the obscured region and not the region itself. This effect is reflected in the different extinctions derived from the $H-K$ optical image and the silicate-based estimate derived from our mid-IR observations, where the peak extinction is about seven times stronger than for the stellar light-based estimate. Our $A_V(9.85\ \mu m)$ is also a factor ~1.7 higher than the extinction ($A_V = 36^{+18}_{-11}$ mag) previously inferred from ISO observations of the [S III] 18.7/33.5 μm line ratio (Spoon et al. 2000). This difference can be explained by the peaked nature of the silicate-based extinction map and occurs because of the larger apertures ($\geq 14'' \times 20''$) of the ISO observations, which averages out the extinction to the lower value.

Figure 9 shows the contour lines of the IRS/SH surface brightness map of the molecular hydrogen line H_2 S(1) 17.0 μm (*top left*), H_2 S(2) 12.3 μm (*top right*), the IRS/SL map of the H_2 S(3) 9.7 μm line (*bottom left*), and the [Ne II] 12.81 μm line (*bottom right*), overlaid on the silicate-based extinction $A_V(9.85\ \mu m)$ map. The molecular hydrogen emission avoids the obscured nucleus and peaks between one and three pixels away from the highest obscuration. Although the H_2 S(2) 12.3 μm (Fig. 6) has a similar distribution as the H_2 S(1) line, its peak emission lies closer (~$2.3''$, one pixel) to the peak obscuration and to the H_2O mega maser than the other H_2 lines.

Since the distribution of the silicate-based extinction $A_V(9.85\ \mu m)$ is similar to that of the stellar light-based extinction $A_V(H-K)$ we think that the mid-IR derived extinction towards the starburst ring may be accurate enough to correct the fluxes of the starburst tracers. That is, the elongated shape of the silicate map indicates that the obscuration is mostly associated with the starburst ring rather than with the line of sight to the AGN, so, the $A_V(9.85\ \mu m)$ map can be used to perform an extinction correction for species whose emission emerge from the disk. Species associated with the AGN (BLR and NLR gas) may be suffering more extinction than the disk does. Therefore, the corrected flux derived for the [Ne V] 14.32 μm only corresponds to the best lower limit we can derive from the current data. Figures 10 and 11 show the same set of maps as in Figs. 5 and 6, but corrected for extinction using the estimated $A_V(9.85\ \mu m)$ map. After correcting for extinction, all the fine-structure emission lines, the average 14.5–15.0 μm continuum, and the PAH features peak at about the same position, that of the H_2O mega maser. The corrected for extinction H_2 lines (Fig. 11) show an offset of ~$2.3''$ (one pixel) with respect to the water maser. However, there is a difference of only $<1''$ between the centroids obtained from a 2D Gaussian profile fit of all the lines.

The integrated flux densities of the co-added spectra from the whole 10×10 aperture of the IRS/SH map (described in Sect. 3) are summarized in Table 1. In this work we include only the fluxes of the most prominent emission lines. These fluxes are larger than those reported by Bernard-Salas et al. (2009), because our 10×10 aperture is larger than the SH staring aperture. In Table 1 we also include the fluxes corrected with the silicate-based extinction $A_V(9.85\ \mu m)$, and the line widths (*FWHM*) as estimated from the Gaussian fit.

Table 1. Line fluxes[a] from the 10×10 pixel (~426×426 pc^2) aperture IRS/SH map.

Line	λ_0[b] [μm]	Flux[c] [10^{-21} W cm^{-2}]	Flux(A_V)[d] [10^{-21} W cm^{-2}]	*FWHM*[e] [km s^{-1}]
[S IV]	10.5105	1.61 0.08	22.03 1.12	382.68 30.54
H_2 0–0 S(2)	12.2786	154.07 1.99	889.94 11.57	525.66 6.23
[Ne II]	12.8135	1201.08 118.85	6026.69 563.35	615.54 32.37
[Ne V]	14.3217	5.34 0.53	27.93 0.64	584.70 15.44
[Cl II]	14.3678	12.82 0.10	66.75 0.53	502.97 4.04
[Ne III]	15.5551	127.01 2.79	741.49 18.03	640.81 12.74
H_2 0–0 S(1)	17.0348	252.60 7.64	1781.25 63.90	549.60 18.12
[S III]	18.7129	74.87 1.37	618.00 10.90	562.71 9.59

Notes. [(a)] Obtained from the co-added spectra of the whole 10×10 aperture of the SH map described in Sect. 3. [(b)] Rest wavelength of the lines. [(c)] The flux densities of each line are given in the first row. The row below shows the corresponding uncertainties. [(d)] Flux density corrected for extinction using an average extinction value $A_V \sim 36$ mag estimated from the silicate-based $A_V(9.85\ \mu m)$ (Sect. 3.4). For [Ne V] this extinction correction may be insufficient. See Sect. 4.4. [(e)] Line width in km s^{-1} obtained from the Gaussian fit. The line profile is not corrected for the instrumental profile, which has an *FWHM* of 500 km s^{-1}.

3.5. Rotation in the nuclear region

Even though the spectral resolution ($R \sim 600$) of the IRS/SH module is relatively low in comparison to the resolution used in most kinematic studies, we used the SH spectra to determine shifts in the velocity of various lines. Pereira-Santaella et al. (2010) have studied the validity of the SH velocity fields by using synthetic spectra. They find that the distortion of the wavelength scale introduced by the telescope pointing uncertainties limits the accuracy of the velocity estimates up to ± 10 km s^{-1}, regardless of the S/N of the spectra, for sources that are neither point sources nor uniformly extended sources (e.g., the nuclear region of NGC 4945). Considering as well the uncertainty in the absolute wavelength calibration (~10% of a pixel), which does depend on the S/N of individual spectra, Pereira-Santaella et al. estimate uncertainties of 10–30 km s^{-1} in the SH velocity fields, and conclude that variations of >20 km s^{-1} in the velocity maps are likely to be real.

The derived velocity fields of the [Ne II] 12.81 μm, [Ne III] 15.56 μm, H_2 0–0 S(1) 17.0 μm, S(2) 12.3 μm, and [Cl II] 14.37 μm lines are shown in Fig. 12. They correspond to the lines with the highest S/N ($\gtrsim 100$) in the SH spectra throughout the whole region mapped, and therefore the velocity fields derived from them are considered to be reliable. We also include the velocity field of the [Ne V] 14.32 μm line, although with a much lower S/N ranging from ~1 to ~100 throughout the map. The pixels with less than a 3σ detection level in the [Ne V] line

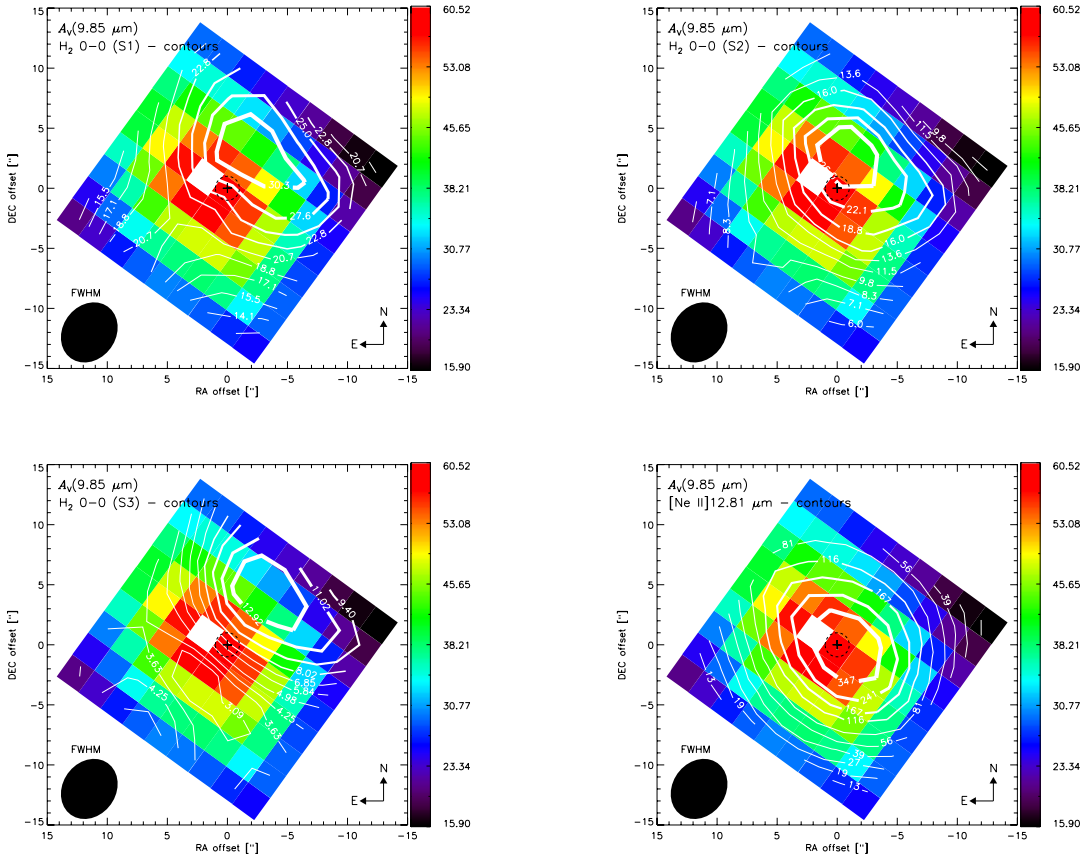

Fig. 9. IRS/SL map of the silicate-based extinction A_V(9.85 μm) with the contour lines of the IRS/SH map of the surface brightness (in units of 10^{-12} W cm^{-2} sr^{-1}) of the molecular hydrogen line H_2 S(1) 17.0 μm (*top left panel*), the IRS/SH map of the H_2 S(2) 12.3 μm line (*top right panel*), the IRS/SL map of the H_2 S(3) 9.7 μm line (*bottom left panel*), and the IRS/SH map of the [Ne II] 12.81 μm (*bottom right panel*). The figures show that the H_2 emission is stronger in a region $\gtrsim$2.3″ away from the peak obscuration, although the H_2 S(2) is the closest to the peak obscuration and to the H_2O mega maser, as well as the [Ne II], which peaks at the H_2O mega maser (within ∼1″), as seen in Fig. 5.

(mostly found at the edges of the map, where the S/N is the lowest) are shown as hatched.

Given that the galaxy major axis runs at PA ∼ 45° and that the inclination of the nuclear disk has been estimated to be less (∼62°) than the inclination (∼80°) of the large-scale galactic disk (Chou et al. 2007), we find that the range of velocities probed in a region of ∼23″×23″ (∼426×426 pc^2) with the [Ne II], [Ne III], and H_2 S(2) lines agree with the range of velocities probed by the ISAAC long slit spectra of the H I Pfβ and H_2 0−0 S(9) lines by Spoon et al. (2003, their Fig.7).

The velocity structure of [Ne II] (*top left panel* in Fig. 12) shows a gradient along the N-S direction rather than NE-SW, as in the case of H_2 0−0 S(1) (*top right panel* in Fig. 12). A similar difference in velocity structure is observed in the [Ne III] and H_2 0−0 S(2) velocity maps (*middle left* and *middle right* panels in Fig. 12, respectively). These different kinematic components may be caused by different origins related to the species emitting, or by different levels of extinction (extinction law at different wavelengths), which allow us to probe deeper regions at one wavelength than another. This is further discussed in Sect. 4.2.

On the other hand, the relatively uniform central region of the [Ne V] velocity field may be due to the lack of spectral resolution and the lower (factor 1 to 100) S/N level obtained in this line. This implies that we are unable to spectrally resolve, at a reliable level, the rather low ($\lesssim$50 km s^{-1}) velocity shifts in the [Ne V] line. Nevertheless, with a higher spectral resolution we would expect a weaker rotation of [Ne V] than the rotation shown by the starburst tracers (from about −120 km s^{-1} to ∼100 km s^{-1}). If the [Ne V] is exclusively related to the AGN NLR, this would mean that the NLR gas does not feel the gravitational pull of the high gas mass inside the starburst ring. But it would feel the pull from the SMBH and not necessarily show the same kinematics as the gas in the starburst ring. In fact, the group of three pixels next (∼43 pc) to the adopted location of the AGN (the H_2O mega maser) shows positive velocities (in the range ∼10−70 km s^{-1} with uncertainties of <1% in the line fit), which is the opposite of the characteristics of the velocity fields of the starburst tracers. This might be a sign of the kinematically decoupled component discovered at the center of the disk with interferometric maps of the $J = 2 \rightarrow 1$ transitions of ^{12}CO, ^{13}CO, and C^{18}O (Chou et al. 2007). However, higher spectral and spatial resolution observations of the [Ne V] line are required to make any reliable conclusion.

4. Discussion

4.1. Tracing the circumnuclear starburst ring

The [Ne II] and [S III] fine-structure lines are our cleanest tracers of star formation (H II regions). If an AGN is present, however, the [Ne III] and [S IV] lines will have contributions from both the starburst and the AGN. In NGC 4945, the AGN contamination to [Ne III] is probably low, given the faintness of [Ne V]. In fact, at the peak flux of the [Ne V] and [Ne III] maps (Fig. 5) the former corresponds to only about 5% of the [Ne III] flux.

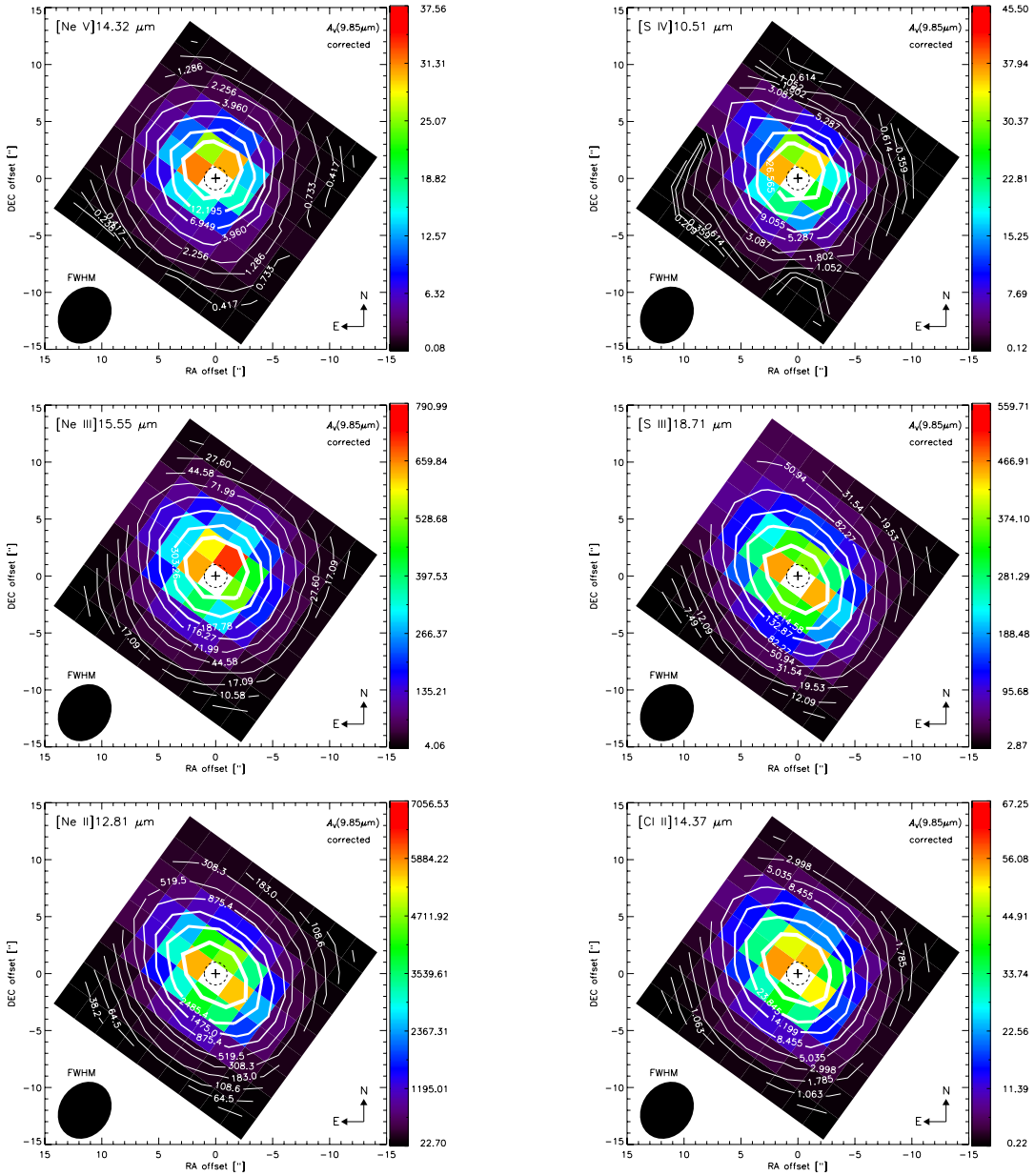

Fig. 10. IRS/SH surface brightness (10^{-12} W cm^{-2} sr^{-1}) maps, corrected for extinction using the extinction law for the local ISM from Chiar & Tielens (2006) and the silicate-based extinction A_V(9.85 μm) (Figs. 8 and 9). The *left panels* show (from top to bottom) the fine-structure lines [Ne V]14.32 μm, [Ne III]15.55 μm, and [Ne II]12.81 μm. The *right panels* show (from top to bottom) the [S IV]10.51 μm, [S III]18.71 μm, and [Cl II]14.37 μm lines. The extinction-corrected fluxes and notations are as in Fig. 5.

From Table 1 we derive the respective luminosities of $L_{[\mathrm{NeV}]} = 7.42 \times 10^{29}$ W sr^{-1} and $L_{[\mathrm{NeIII}]} = 1.76 \times 10^{31}$ W sr^{-1}, using a luminosity distance $D_L = 3.82$ Mpc. However, from the relation between $L_{[\mathrm{NeV}]}$ and $L_{[\mathrm{NeIII}]}$ by Gorjian et al. (2007) (which holds for a group of Seyfert 1 and 2, AGNs, ULIRGs and radio galaxies), the predicted [Ne III] luminosity should be $\sim 3.28 \times 10^{30}$ W sr^{-1}, which is a factor ~5.4 lower than observed. This means that NGC 4945 makes a slightly lower AGN contribution to the [Ne III] line than the outlier NGC 3079 found in the sample by Gorjian et al. (2007), for which the [Ne III] luminosity is a factor ~5 brighter than expected based on its [Ne V] luminosity.

The [Ne III] 15.56/[Ne II] 12.81 μm line ratio (Fig. 13) ranges between ~0.13 and ~0.27 above and below the major axis of the region mapped. The difference with the lowest ratios (0.06–0.13), which are found along the northeast-southwest axis, is more pronounced than in the [Ne V] 14.32/[Ne II] 12.81 μm line ratios (*top left panel* in Fig. 13).

The lowest [Ne III] 15.55 μm/[Ne II] 12.81 μm line ratios coincide with the 100 pc-scale circumnuclear starburst ring of NGC 4945 (*bottom panels* in Fig. 14), detected in Paα emission with HST NICMOS (Marconi et al. 2000). The increasing gradient above the starburst ring seems to mimic the conical-shaped cavity traced by the H_2 1–0 S(1) line (Marconi et al. 2000). However, the ratio also increases toward the southeast direction from the starburst ring, which instead implies that the ring has different properties than its surroundings.

In fact, a similar increase in [Ne III]/[Ne II] ratios away from the nucleus is observed in the nuclear maps by Pereira-Santaella et al. (2010, their Fig. 5), with the exception of NGC 7130, the only galaxy classified as LINER/Seyfert 2 in their sample. According to (Snijders et al. 2007), the higher

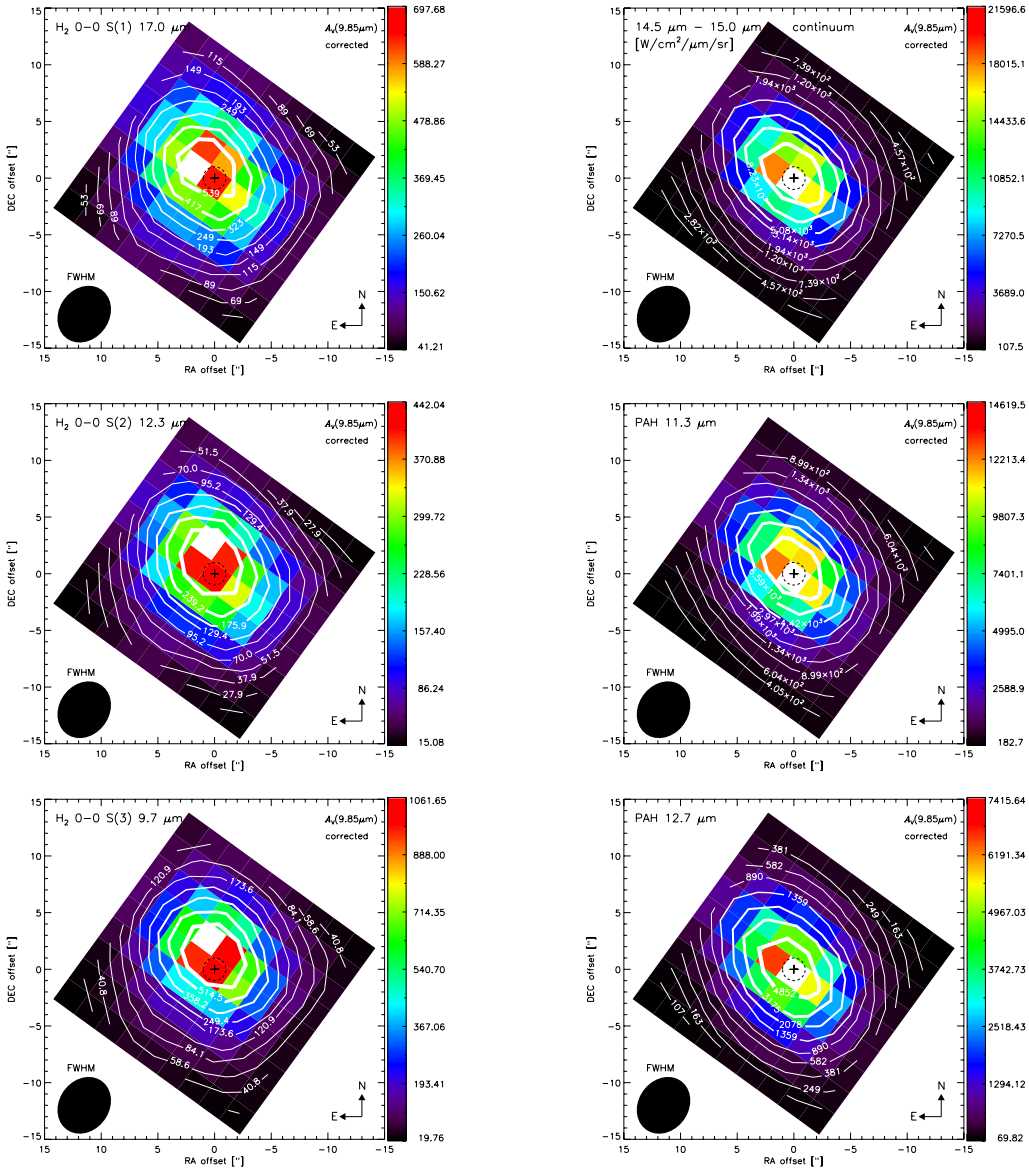

Fig. 11. IRS/SH surface brightness (10^{-12} W cm^{-2} sr^{-1}) maps, corrected for extinction using the extinction law for the local ISM from Chiar & Tielens (2006) and the silicate-based extinction $A_V(9.85\,\mu m)$ (Figs. 8 and 9). The molecular hydrogen lines H_2 S(1) 17.0 μm, H_2 S(2) 12.3 μm, and H_2 S(3) 9.7 μm (from the IRS/SL map) are shown in the *left panel*. The *right panel* shows (from top to bottom) the average continuum flux density (10^{-12} W cm^{-2} μm^{-1} sr^{-1}) between 14.5 μm and 15.0 μm, and the the surface brightness (10^{-12} W cm^{-2} sr^{-1}) of the PAH features at 11.3 μm and 12.7 μm. The extinction-corrected fluxes and notations are as in Fig. 5.

the metallicity, the higher the age of the stellar population, and the higher the gas density, the lower should be the [Ne III] 15.55 μm/[Ne II] 12.81 μm ratio.

The [S III] 18.71/[Ne II] 12.81 line ratio is considered a good tracer of densities in the range 10^4 and 10^6 cm^{-3} because their similar excitation potentials (21.6 eV and 23.3 eV, for [Ne II] and [S III], respectively) and significantly different critical densities (6.1×10^5 cm^{-3} for [Ne II] and 1.0×10^4 cm^{-3} for [S III]) make this ratio less sensitive to the hardness of the radiation field than to the density of the ISM. According to the models by Snijders et al. (2007), a lower [S III]/[Ne II] ratio would indicate higher densities. In Fig. 13 the [S III] 18.71/[Ne II] 12.81 line ratios are also lower in the center than around it. This ratio ranges between 0.002 and 0.013 in the center, which indicate densities larger than 10^6 cm^{-3} in a >5 Myr old starburst system with solar metallicity and relatively high ($q = 8 \times 10^8$) ionization parameter (Snijders et al. 2007, their Fig. 5). Based on our observed [Ne III]/[Ne II] ratios, the [S III]/[Ne II] ratios predicted using the model by Pereira-Santaella et al. (2010, their Eq. (2)) are about ten times higher than the observed ratios. These can be a consequence of the about ten times higher extinction found in NGC 4945 than in the sample of galaxies used by Pereira-Santaella et al. (2010).

The [Ne III]/[Ne II] line ratios obtained with the extinction correction (*middle right panel* in Fig. 13) are just ~9% higher than without correction. This relatively small change after the extinction correction is because, even in a high-extinction situation, the differential extinction between [Ne III] and [Ne II] is small, given that both lines are closely spaced in wavelength and not in one of the silicate absorption features. On the other hand, because of their larger differential (wavelength) extinction, the [S III]/[Ne II] ratios corrected for extinction do change significantly from a factor ~50 in the center (where the extinction is higher) to a factor 3 away from the center (where the extinction is lower).

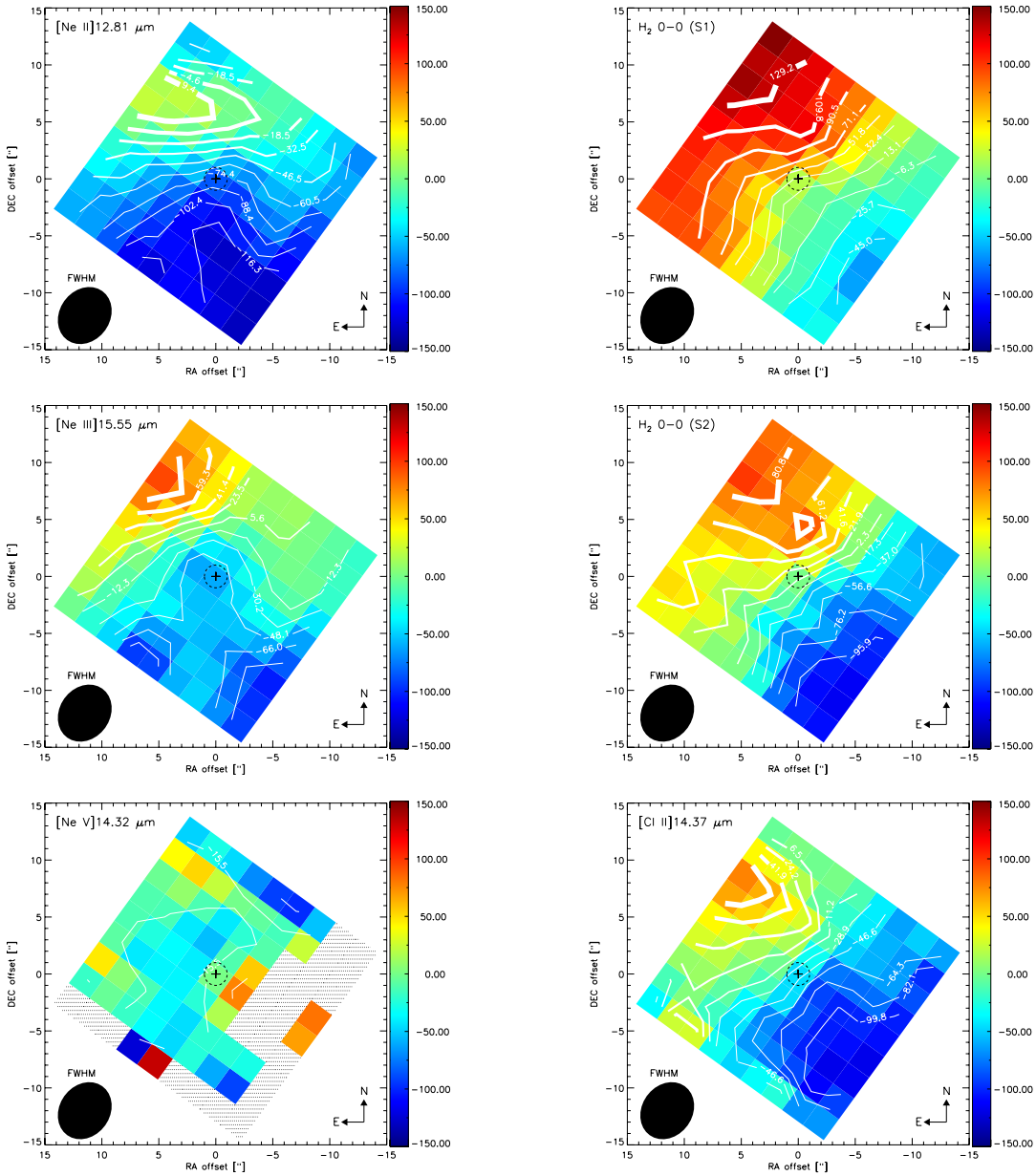

Fig. 12. The *left panel* shows (from top to bottom) the velocity fields of the fine-structure lines [Ne II] 12.81 μm, [Ne III] 15.56 μm, and [Ne V] 14.32 μm. The *right panel* shows (from top to bottom) the molecular hydrogen lines H_2 0−0 S(1) 17.0 μm, along with S(2) 12.3 μm, and the [Cl II] 14.37 μm. The maps, covering a region of ~23″ × 23″ (~426 × 426 pc^2), are consistent with a rotating disk, with the exception of the [Ne V] line, which presents a relatively uniform (most likely not spectrally resolved) velocity field.

Only the ratios from our co-added fluxes (Table 1) can be compared to other galactic nuclei, since the 10 × 10 aperture is comparable to the size probed in any of the more distant galaxy nuclei. The [Ne III]/[Ne II] ratio at the position of the H_2O mega maser is about 10% lower than the ratio obtained from the fluxes of the 10 × 10 co-added spectrum (Table 1).

Since in starburst environments the [Ne II] and [Ne III] emission lines are expected to be driven mainly by photo-ionization (e.g., Ho & Keto 2007), the lower ratios found along the northeast-southwest axis are likely due to a [Ne II] emission enhanced by the starburst ring. Despite this, these low ratios are also consistent with a ratio [Ne III]/[Ne II] ≤ 0.1 found in shocks (Binette et al. 1985) where the low ionization line [Ne II] can also be enhanced (Voit 1992).

On the other hand, the highest [Ne III]/[Ne II] ratios found above and below the starburst ring are greater than those typically found in shocks. These higher ratios could actually be tracing an additional contribution to the [NeIII] emission by a conically shaped narrow-line region (NLR). Previously, no evidence was found for the existence of such an NLR, given the absence of 5007 Å [O III] emission in the central 800 pc × 800 pc (Moorwood et al. 1996b). Instead, the conical cavity traced by optical and near-infrared line and continuum tracers (Moorwood et al. 1996b; Marconi et al. 2000) was associated with a starburst super wind. However, given the high extinction implied by our observations, optical [O III] emission can be easily attenuated, mid-infrared [Ne III] emission less so. A hypothetical conical NLR would be difficult to identify from an [Ne III] map alone due to blending with the nuclear starburst component. But it may manifest itself more clearly in an [Ne III]/[Ne II] map, in which the contribution of the starburst component diminishes quickly beyond the nucleus proper.

The [Ne III]/[Ne II] ~ 0.06−0.13 ratios observed along the starburst ring agree closely with the ratios observed in some

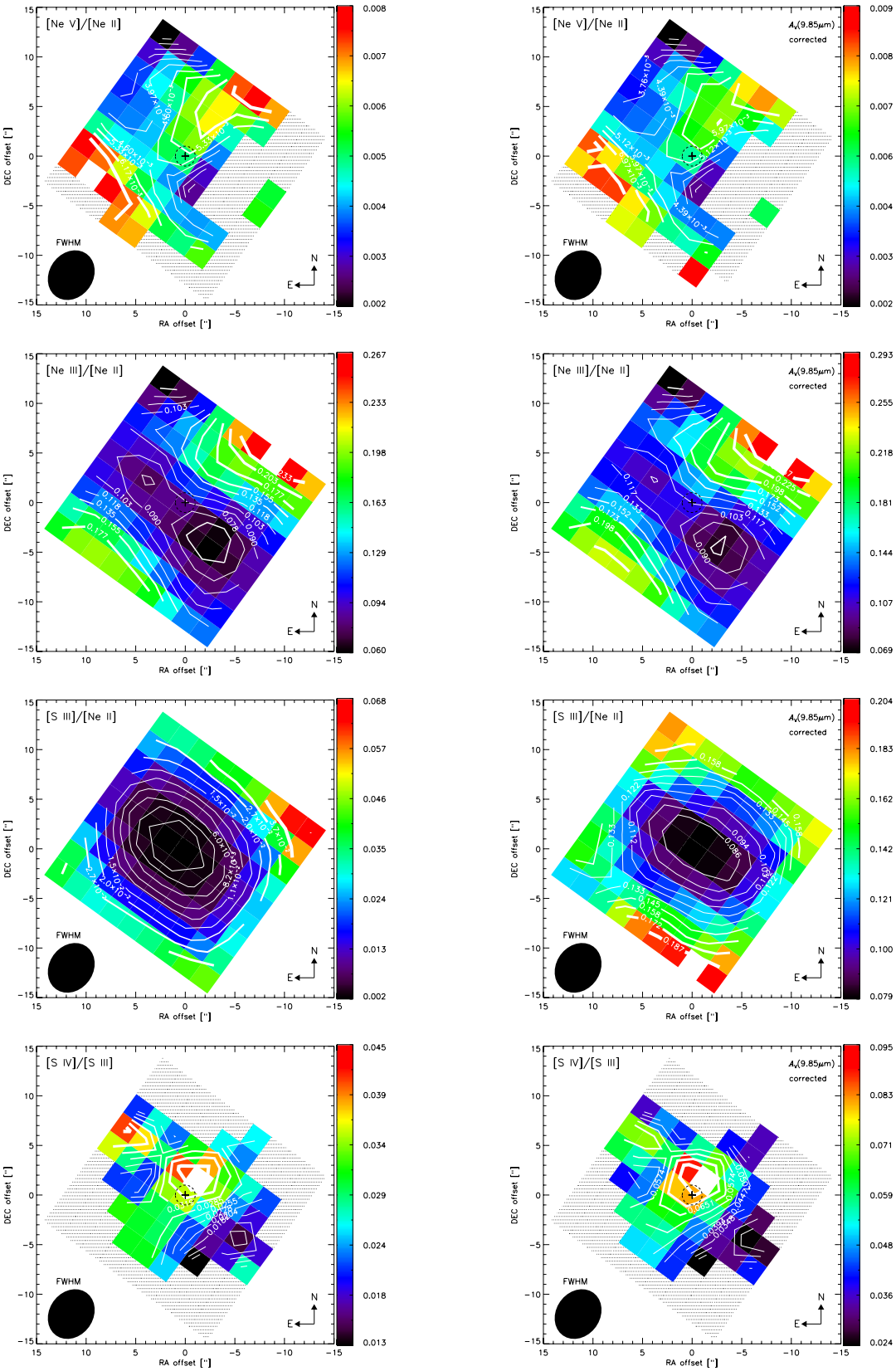

Fig. 13. *Left panels* – Integrated flux ratios between the fine-structure lines (from top to bottom) [Ne V] 14.32/[Ne II] 12.81, [Ne III] 15.56/[Ne II] 12.81, [S III] 18.71/[Ne II] 12.81, and [S IV] 10.51/[S III] 18.71. *Right panels* – Same as above, but considering the fluxes corrected for extinction. The hatched areas correspond to pixels with a $<3\sigma$ detection level in the faintest emission lines [Ne V] 14.32 μm and [S IV] 10.51 μm.

galaxies of the ISO starburst sample and are consistent with burst timescale models predicting a relatively short-lived starburst of 5−8 Myr (Thornley et al. 2000, their Fig. 6). In the whole region mapped, we observe ratios [Ne III]/[Ne II] < 0.3, which

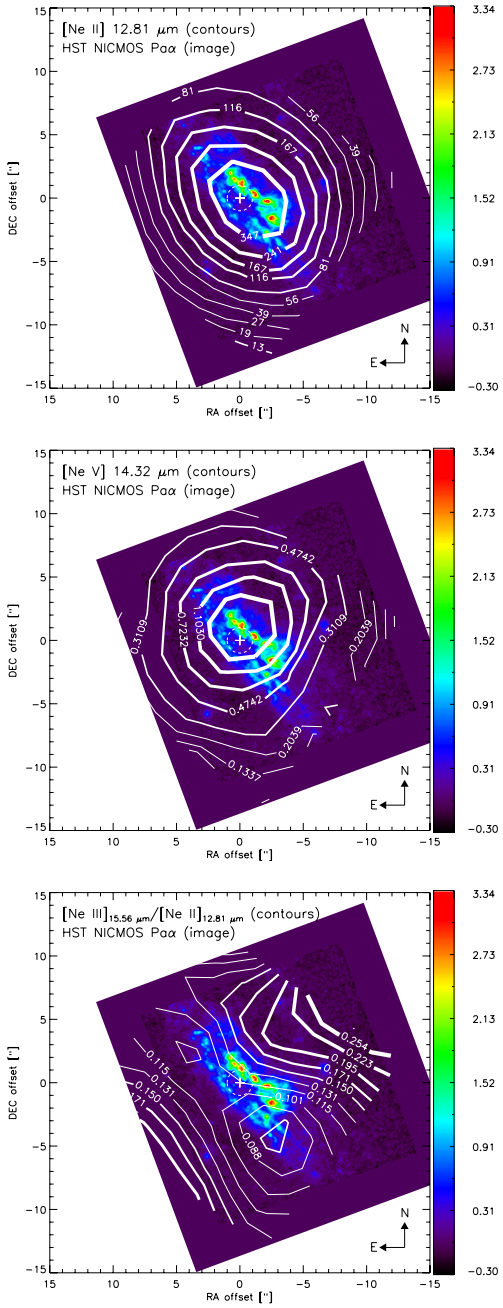

Fig. 14. HST NICMOS image of Paα (in units of 10^{-21} W cm^{-2}) of the nucleus of NGC 4945 (Marconi et al. 2000). The contours not corrected for extinction (labelled in units of 10^{-12} W cm^{-2} sr^{-1}) are the fine-structure lines [Ne II] 12.81 μm (*top panel*) and [Ne V] 14.32 μm (*middle panel*). The [Ne V] flux peaks at about one pixel to the northwest of the H_2O mega maser (Fig. 5), The *bottom panel* shows the [Ne III] 15.55/[Ne II] 12.81 μm line ratio not corrected for extinction.

are a factor ~3 lower than the ratios observed in the sample of quasars reported by Veilleux et al. (2009). However, the ratio [Ne III]/[Ne II] ~ 0.07 observed at the nucleus of NGC 4945 is comparable to the ratios observed in the nucleus of five (out of 16) galaxies in the sample of LIRGs studied in Pereira-Santaella et al. (2010, their Fig. 14).

On the other hand, the differential extinction between [S III] and [S IV] is greater than between [Ne II] and [Ne III]. Because [S IV] sits close to the deepest point of the silicate absorption feature at 9.7 μm (Fig. 2), the [S IV] 10.51/[S III] 18.71 μm line ratios corrected for extinction (*bottom right* in Fig. 13) are a factor ~2 more than those obtained without correction (*bottom left* in Fig. 13). In both cases the highest ratio is found about 2.3″ (one pixel) northwest of the H_2O mega maser. The map-averaged ratios uncorrected for extinction (from the fluxes in Table 1) of [Ne III]/[Ne II] ~ 0.11 and [S IV]/[S III] ~ 0.02 are similar (within 10%) to the ratios obtained from the SH staring observations by Bernard-Salas et al. (2009). They position NGC 4945 among the sources with the lowest hardness of the radiation field in their sample of starburst galaxies, which, according to Bernard-Salas et al., may indicate an old (or small) population of massive stars in NGC 4945. However, this can only be concluded for the outermost surface that we can probe with [S IV] and [S III] lines, and we cannot rely much on the extinction corrected data for this analysis, since the [S IV]/[S III] ratio depends more on the extinction law used than the [Ne III]/[Ne II] ratio.

4.2. Molecular hydrogen gas

As can be seen in Figs. 5 and 6, the emission centroids of the H_2 0−0 S(1), S(2), and S(3) lines are clearly offset from the centroids of the low ionization fine-structure lines, which all peak close to the H_2O mega maser. Such an offset would be hard to understand if the H_2 0−0 S(1), S(2), and S(3) lines and the HII region gas were exposed to similar amounts of extinction. The differential extinction between H_2 S(2) and [Ne II] at 12.28 and 12.81 μm, for instance, is very small. The same is true for the wavelengths of H_2 S(1) at 17.0 and [S III] at 18.71 μm. The lack of H_2 0−0 S(1), S(2), and S(3) emission at the position of the mega maser can be explained if the molecular hydrogen emission in the nucleus is more strongly attenuated than the HII region gas. That is, the inner H_2 emission would suffer additional/differential extinction that is not accounted for by the silicate feature. On the other hand, analysis of the higher pure rotational lines observed in the SL module (Spoon et al., in prep.) and with VLT-ISAAC (Spoon et al. 2003, their Fig. 7) indicates that the S(5), S(7), and S(9) lines originate progressively closer to the nucleus. This seems hard to reconcile with the above scenario, given that $A(\lambda)/A_V$ in the S(5)−S(9) wavelength range is likely higher than in the S(1)-S(2) wavelength range.

We instead favor a scenario in which the lower pure rotational lines S(1) and S(2) mainly originate in an unobscured extra-nuclear component associated with the super-wind cone as seen in the HST NICMOS map of the vibrational H_2 1−0 S(1) emission (Marconi et al. 2000). Figure 15 shows the IRS/SH maps of the pure rotational H_2 S(1) and S(2) lines overlaid on the H_2 1−0 S(1) map. Interestingly, the two pure rotational lines peak farther from the apex of the cone than the 1−0 S(1) line does, the 0−0 S(1) line (upper level energy 1015 K) more so than the 0−0 S(2) line (T_{up} = 1682 K). In this scenario the higher pure rotational lines S(5), S(7), and S(9) would originate mainly in the starburst ring or within. There one likely finds the high critical densities (n_{crit} > 10^5 cm^{-3}), as well as high gas temperatures (T_K > 10^3 K) needed to thermalize these lines (as seen in active galaxies such as NGC 1068, Mrk 231, and Arp 220; e.g. Pérez-Beaupuits et al. 2007, 2009; Aalto et al. 2007; van der Werf et al. 2010), but they will also be affected by strong extinction. This strong extinction may cause the nuclear component of the 2.12 μm H_2 1−0 S(1) line (T_{up} = 6950 K) to suffer far more extinction than the longer wavelength H_2 0−0 S(5)−S(9) lines and therefore to be associated solely with the conical cavity. In all of this the H_2 0−0 S(3) line, originating at an upper level energy of 2500 K, may have both strong nuclear and cavity components. Owing to the extreme extinction

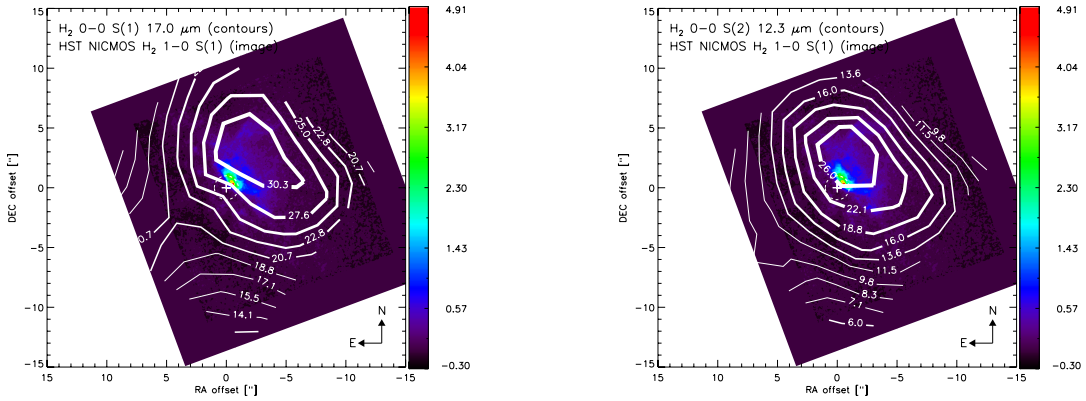

Fig. 15. IRS/SH contours of the rotational H_2 0−0 S(1) (*left*) and H_2 0−0 S(2) (*right*) lines overlaid on the HST NICMOS map of the vibrational H_2 1−0 S(1) molecular hydrogen line (Marconi et al. 2000).

the nuclear component would be suppressed, leaving only the cavity component for us to see.

4.3. Excitation of H_2

For LTE conditions and an ortho-to-para ratio of three (Neufeld et al. 2006, their Fig. 13), we can estimate the excitation temperature of the molecular hydrogen throughout the region mapped with the IRS/SH module, from the ratio between the flux of the H_2 0−0 S(2) 12.3 μm and H_2 0−0 S(1) 17.0 μm lines as

$$T_{\rm ex} = -\frac{T_{\rm up}^{\rm S(2)} - T_{\rm up}^{\rm S(1)}}{\log(F_{\rm S(2)}\nu_{\rm S(1)}A_{\rm S(1)}g_{\rm S(1)}) - \log(F_{\rm S(1)}\nu_{\rm S(2)}A_{\rm S(2)}g_{\rm S(2)})} \quad {\rm K}, \tag{4}$$

where $F_{\rm S(1)}$ and $F_{\rm S(2)}$ are the integrated flux densities of the H_2 0−0 S(1) and S(2) lines, ν the corresponding rest frequency ($\sim 1.75 \times 10^{13}$ Hz for S(1) and $\sim 2.44 \times 10^{13}$ Hz for S(2)), and A and g are the respective Einstein A-coefficients and statistical weights of each transition. The upper level energy $T_{\rm up}$ of the transitions is in units of K.

Figure 16 shows the IRS/SH maps (not corrected for extinction) of the H_2 0−0 S(2) to S(1) total flux ratio (*top left panel*) and the corresponding map of the excitation temperature $T_{\rm ex}$ (K) (*bottom left panel*) of the molecular hydrogen, estimated from Eq. (4). The peak excitation temperature of $\sim$528 ± 31 K is reached $\gtrsim$2.3″ (one pixel) to the north of the H_2O mega maser. The *right hand panels* of Fig. 16 show the H_2 0−0 S(2)/S(1) ratio and the estimated excitation temperature from the respective H_2 fluxes corrected for extinction with the silicate-based $A_{\rm V}$(9.85 μm). The correction for extinction leads to a peak temperature of 421 K, which is about 100 K lower than the temperature derived from the uncorrected fluxes. However, the distribution of the temperature and the position of its peak value do not change.

Since galaxies are complex systems, the H_2 gas is not expected to be at any single temperature. Besides, a long line of sight can probe different excitation environments (e.g., PDRs, XDRs, shocks) as in the sample of galaxies studied by Roussel et al. (2007). Previous estimates of the excitation temperature, based on SWS observations of the (0−0) S(0) and S(1) fluxes detected in the nucleus of NGC 4945, have led to a cooler H_2 component with $T_{\rm ex} \sim 160$ K (corresponding to about 9% of the total H_2 mass), while a temperature $T_{\rm ex} \sim 380$ K (about 0.4% of H_2 mass) was estimated from the S(1) and S(2) fluxes (Spoon et al. 2000, their Table 6), which is in close agreement with our result considering the size of the big SWS slit. This excitation temperature is similar to the temperature $T_{\rm ex} = 365 \pm 50$ K derived for the low-energy transitions in NGC 1377 (Roussel et al. 2006), but higher than the temperature of $T_{\rm ex} = 292 \pm 6$ K estimated from the S(0)−S(3) lines observed in NGC 6240 (Higdon et al. 2006).

Since we cannot use the map of the H_2 S(3) 9.7 μm line due to the flux mismatch between the SH and SL modules mentioned in Sect. 3, we would only be able to base our estimate of the warm H_2 mass on the S(1) and S(2) lines. In fact, even if we had been able to use the S(3) line, most of the mass is revealed by including the S(0) line. This line has, however, not been mapped, since the spatial resolution of the LH module is much lower than that of the SH and SL modules.

4.4. AGN-dominated [Ne V] emission?

The detection of [Ne V] emission from the nucleus of NGC4945 is not surprising. The galaxy hosts a 1.4×10^6 $M_\odot$ supermassive black hole, as revealed by H_2O maser observations (Greenhill et al. 1997) with an intrinsic 0.1−200 keV luminosity of 1.8×10^{43} erg s^{-1} (Guainazzi et al. 2000).

More remarkable is the faintness of the [Ne V] emission. Only 10^{-6} of the infrared luminosity of the galaxy is detected in the [Ne V] line (Table 1). This is surprisingly little for an AGN which can easily account for the entire bolometric emission of the galaxy (Marconi et al. 2000). It is also 100 times less than L([Ne V])/$L_{\rm IR}$ for galaxies whose IR luminosity is dominated by AGN activity (Goulding & Alexander 2009).

Interesting is also the size of the [Ne V] emitting region, which can be reasonably well constrained given that one arcsecond corresponds to 18.5 pc. at a distance of 3.82 Mpc. Since the spatial profile of the [Ne V] map (Fig. 5) is only marginally wider than the PSF, the radius of the [Ne V] emitting region will be less than 55 pc ($\sim$3″). This upper limit is higher than the size of coronal line regions (e.g. $\sim$19 pc for Circinus as probed by the 2.48 μm [Si IV] line; Prieto et al. 2004), but lower than the kpc scale of narrow line regions as probed with [O III] (e.g. Circinus; Marconi et al. 1994).

Both the faintness and the observed extent of the [Ne V] emission are likely to be affected by strong extinction within the nucleus. However, if the narrow line region were to extend above the plane of the molecular disk in which the AGN and the circumnuclear starburst are embedded, the amount of extinction would be less than probed by the silicate absorption feature ($A_{\rm V} = 50-60$). The amount will, however, certainly be

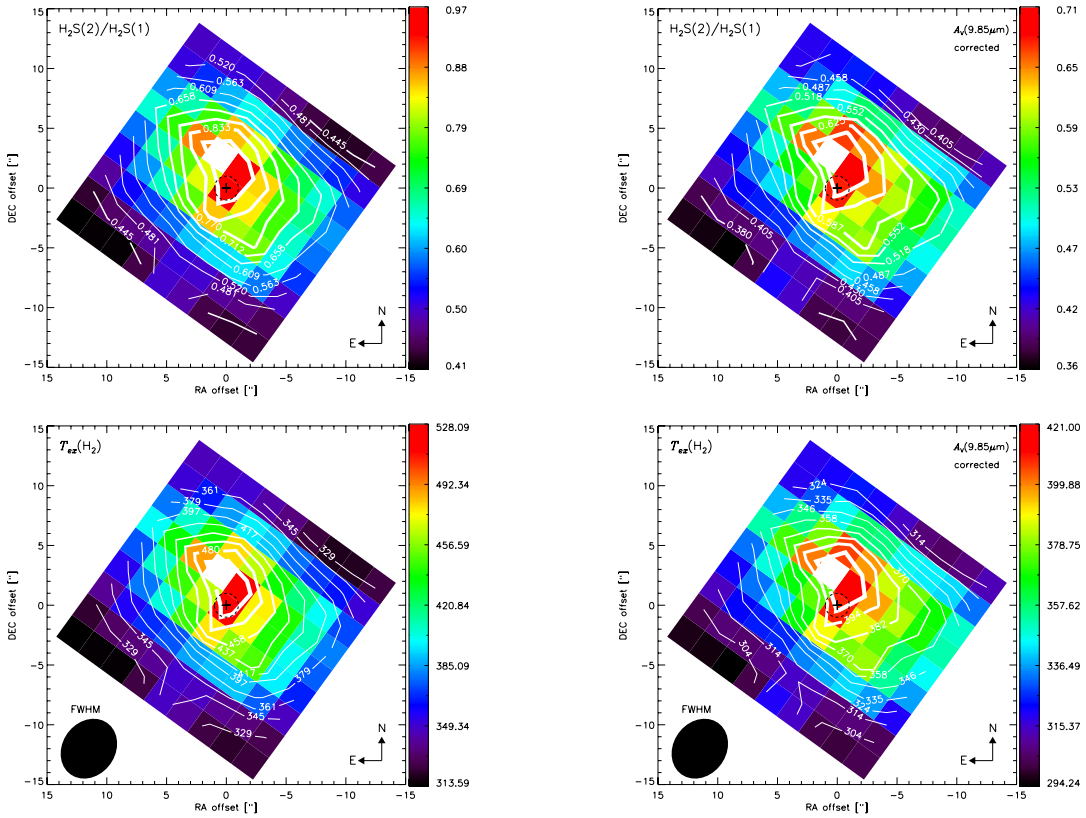

Fig. 16. *Left panels* – IRS/SH maps of the H_2 0–0 S(2) to H_2 0–0 S(1) total flux ratio (*top left panel*), and the map of the estimated T_{ex} (K) of the molecular hydrogen. The peak excitation temperature of ∼528 K is reached about $\gtrsim$2.3″ (one pixel) to the north of the H_2O mega maser. *Right panels* – Same as above, but using the extinction corrected fluxes of the H_2 S(2) and S(1) lines. The extinction correction leads to an ∼100 K lower peak temperature.

less than the line of sight extinction to the AGN broad line region, $N_H = 2.4 \times 10^{24}$ cm^{-2} (Guainazzi et al. 2000), which is equivalent to $A_V = 1300$.

The extinction probed by the silicate absorption feature is consistent with the F([Ne V])/F(14−195 keV) ratio found for Sy1 galaxies (Weaver et al. 2010) when multiplied by the absorption corrected 14−195 keV flux for NGC 4945. This flux depends on the geometry of the absorber, and ranges between five and ten times the Swift-BAT flux of NGC 4945 ($F(14-195\,\mathrm{keV}) = 33 \pm 0.8 \times 10^{-18}$ W cm^{-2}; Tueller et al. 2010) for a spherical and edge-on disk geometry, respectively (K. Iwasawa, priv. comm.). Taking the factor 2.5 scatter further into account in the F([Ne V])/F(14−195 keV) ratio for Sy1 galaxies, the attenuation on the [Ne V] flux ranges between 12 and 157, which corresponds to $A_V = 55-112$ mag for our adopted local ISM extinction law of Chiar & Tielens (2006). This result would indicate that the NLR is buried along with the other components of the nuclear molecular disk.

The strong obscuration to the NLR in NGC 4945 may serve as a warning that mid-infrared NLR tracers such as [Ne V] and [O IV] may not always be suitable as tracers of the AGN luminosity as suggested by Goulding & Alexander (2009). Galaxies in this risk group may be recognized by the presence of a deep silicate absorption feature in their mid-infrared spectra and a classification 3A, 3B or 3C in the mid-infrared galaxy classification scheme of Spoon et al. (2007). Besides NGC 4945 galaxies in this group include LIRGs such as NGC 4418 and ULIRGs like Arp 220, IRAS 08572+3915 and IRAS F00183-7111.

The example of NGC 4945 may also serve as a warning that not detecting NLR tracers in AGN does not necessarily imply the absence of an NLR. Instead it may indicate that the NLR is so strongly attenuated that the line does not emerge above the continuum noise. In these cases, only deep mid-IR observations, like the ones presented here, would reveal these tracers.

In NGC4945 the [Ne V] line was detected at 5% of the continuum flux in a spectrum with continuum S/N of 140 in the 14−15 μm range. Other galaxies that may host an AGN and which have been observed at similar S/N (among them ULIRGs like Arp220 and IRAS 08572+3915) do not show evidence of [Ne V] emission (Armus et al. 2007). The NLR in these galaxies may then be even more strongly obscured than in NGC 4945, or the AGN may contribute a far smaller fraction of the bolometric power than in NGC 4945. The NLR may also simply not exist if the ionizing photons needed to form the NLR are 4π-obscured close to their origin.

4.5. [Ne V] emission from supernovae? The template Cassiopeia A

Although the [NeV] emission is unresolved along the major axis and only marginally resolved along the minor axis (as discussed in Sect. 3), that the [Ne V] line has also been observed in supernova remnants (SNRs) (e.g. Oliva et al. 1999; Smith et al. 2009) raises valid questions: could the [Ne V] emission observed in NGC 4945 be powered purely by SNRs? If so, how many SNRs would be needed to reproduce its [Ne V] flux? As in Modica et al. (2010), we explore below the alternative of [Ne V] emission being powered by the SNRs in the nuclear region of NGC 4945. We note, though, that the number of supernovae needed depends

not only on the total [Ne V] flux but also on the actual size of the SNR.

Our analysis is based on previous *Spitzer*/IRS SL module observations of Cassiopeia A (Cas A) from which the global distribution of fine-structure lines covering a 5.3×5.3 arcminute^2 area was presented by Smith et al. (2009). The total [Ne V] flux of Cas A was not reported before due to the difficulties to extract the flux with enough reliability. Using fitting techniques tailored to the [Ne V] line, we now are able to state its total flux as $1.5 \pm 0.7 \times 10^{-18}$ W cm^{-2}. Considering an average extinction $A_V \sim 5$ mag (Hurford & Fesen 1996), and using the extinction law for the local ISM by Chiar & Tielens (2006), the corrected flux is $\sim 1.9 \pm 0.9 \times 10^{-18}$ W cm^{-2}.

On the other hand, the total [Ne V] flux in NGC 4945 is $\sim 5.3 \pm 0.5 \times 10^{-21}$ W cm^{-2}. To estimate the dereddened [Ne V] emission observed in NGC 4945, we computed an average extinction value $A_V \sim 36$ mag from the $A_V(9.85\,\mu\mathrm{m})$ map (Fig. 8). Owing to the stronger extinction at the central pixels, this only represents a lower limit to the actual extinction on the [Ne V] line. Thus the lower limit for the extinction-corrected total [Ne V] flux is $\sim 27.9 \times 10^{-21}$ W cm^{-2}.

Considering a canonical distance of 3.4 kpc for Cas A (Smith et al. 2009, and references therein) and ~3.82 Mpc for NGC 4945, we found that the ratio between the total [Ne V] flux of NGC 4945 and Cas A, corrected by the square of the ratio between the distances $(D_{\mathrm{NGC4945}}/D_{\mathrm{CasA}})^2$, is about 19×10^3. This represents a lower limit to the number of contemporaneous Cas A type supernovae needed to produce the extinction-corrected [Ne V] emission observed in NGC 4945. Another extreme lower limit can be obtained by assuming no extinction in the NGC 4945 flux, from which the same exercise indicates that about 4×10^3 Cas A type SNRs would be needed.

According to Lenc & Tingay (2009), the upper limit to the supernova rate in NGC 4945 is 15.3 yr^{-1}, which means the individual supernovae, for the uncorrected and lower limits corrected for extinction estimated above, need to emit at Cas A levels for about 260 and 1240 years, respectively. These are reasonable numbers given that the age of Cas A is estimated to be about 330 yr (Fesen et al. 2006), while the kinematic age of another [Ne V] emitting SNR, E0102, has been estimated to be 2050±600 yr (Finkelstein et al. 2006). This implies that the number of SNRs estimated above can indeed persist long enough to power the [Ne V] emission observed in NGC 4945, at least from the point of view of the SNR properties used in our estimate. However, Lenc & Tingay (2009, their Sect. 4.5) also determine a median SN age of 85 yr, which translates into a median supernova rate of ~0.12 SNe/yr, or a much (15.3/0.12 ~ 128 times) longer radiative phase ($\sim 3-16 \times 10^4$ years) needed for the individual supernovae. Therefore, the [Ne V] flux observed in NGC 4945 is likely not powered by a population of supernova remnants.

5. Final remarks

We have mapped the central region of NGC 4945 with the SH and SL modules of the *Spitzer* InfraRed Spectrograph. From the SH spectral cubes we produced maps of fine-structure emission lines [S IV] at 10.51 μm, [Ne II] at 12.81 μm, [Cl II] at 14.37 μm, [Ne III] at 15.56 μm, [S III] at 18.71 μm, the AGN narrow-line region tracer [Ne V] at 14.32 μm, and the molecular hydrogen lines, H_2 S(2) at 12.3 μm and H_2 S(1) at 17.0 μm. From the SL spectral cubes we obtained maps of the H_2 S(3), and the silicate absorption feature at 9.7 μm.

We presented the first map of [Ne V] 14.32 μm towards the nucleus of NGC 4945 with flux detection levels down to 0.1×10^{-12} W cm^{-2} sr^{-1} per pixel. We produced and estimated an extinction map $A_V(9.85\,\mu\mathrm{m})$ based on the apparent strength of the 9.7 μm silicate absorption feature, which traces the contours of the starburst ring at a ~5″ spatial resolution.

Most of the emission lines are found to peak on the nucleus, within the uncertainty of the astrometry. Only the warm molecular hydrogen emission shows a maximum about 60–100 pc NW of the nucleus. After correction for extinction, the distribution of the H_2 rotational emission is more concentrated in the nuclear region, but its peak emission is still slightly offset from the peak of the other emission lines, that of the H_2O mega maser. Thus, we favor a scenario in which the lower pure rotational lines S(1) and S(2) mainly come from an unobscured extra-nuclear component associated with the super-wind cone as seen in the HST NICMOS map of the vibrational H_2 1−0 S(1) emission, with an intrinsic excitation trend toward the nucleus, which is reflected in the higher level S(5)−S(9) lines.

We found that the map-integrated [Ne V]/[Ne II] ratio is consistent with ratios observed in starbursts rather than in AGNs. The [Ne III]/[Ne II] < 0.13 ratios observed along the starburst ring are likely due to an excess [Ne II] emission driven by the starburst ring or to high density (>10^6 cm^{-3}) ISM gas in the circumnuclear disk.

A range of extinction $A_V \sim 55-112$ mag (which corresponds to an attenuation of a factor 12−160) estimated for [Ne V] from our observed [Ne V] flux and the absorption-corrected 14−195 keV Swift-BAT flux, indicate that mid-infrared NLR tracers such as [Ne V] and [O IV] may not be trusted as tracers of the AGN luminosity of galaxies with a deep silicate absorption feature.

A new estimate of the total [Ne V] flux in Cassiopeia A indicates that at least $4-19 \times 10^3$ Cas-A type supernova remnants, with ages between >260 (no extinction correction) and >1240 (on extinction correction) years, would be needed to power the [Ne V] emission observed in NGC 4945. However, given the actual median age of SNRs observed in NGC 4945 and the uncertainty in the true extinction of its [Ne V] emission, SNRs are not likely to fully reproduce the [Ne V] flux observed in the nucleus of this galaxy.

Acknowledgements. We thank Varoujian Gorjian for the *Spitzer*-MIPS 24 μm map of the central region of NGC 4945. We also thank Alessandro Marconi for providing the HST NICMOS images, and Emil Lenc for the ATCA 2.3 GHz image. We thank Kazushi Iwasawa for the very useful comments and the correction factors provided for the SWIFT-BAT fluxes. We are grateful to Aleks Diamond-Stanic for constructive discussions. We also thank the referee for his/her pertinent and insightful comments. We are also grateful to the SPITZER/SINGS team for their support during and after the observations.

References

Aalto, S., Booth, R. S., Black, J. H., & Johansson, L. E. B. 1995, A&A, 300, 369
Aalto, S., Spaans, M., Wiedner, M. C., & Hüttemeister, S. 2007, A&A, 464, 193
Alonso-Herrero, A., Rieke, G. H., Colina, L., et al. 2009, ApJ, 697, 660
Armus, L., Charmandaris, V., Bernard-Salas, J., et al. 2007, ApJ, 656, 148
Baum, S. A., Gallimore, J. F., O'Dea, C. P., et al. 2010, ApJ, 710, 289
Bernard-Salas, J., Spoon, H. W. W., Charmandaris, V., et al. 2009, ApJS, 184, 230
Binette, L., Dopita, M. A., & Tuohy, I. R. 1985, ApJ, 297, 476
Brandl, B. R., Bernard-Salas, J., Spoon, H. W. W., et al. 2006, ApJ, 653, 1129
Brock, D., Joy, M., Lester, D. F., Harvey, P. M., & Ellis, Jr., H. B. 1988, ApJ, 329, 208
Chiar, J. E., & Tielens, A. G. G. M. 2006, ApJ, 637, 774
Chou, R. C. Y., Peck, A. B., Lim, J., et al. 2007, ApJ, 670, 116
Done, C., Madejski, G. M., & Smith, D. A. 1996, ApJ, 463, L63

Farrah, D., Bernard-Salas, J., Spoon, H. W. W., et al. 2007, ApJ, 667, 149
Fesen, R. A., Hammell, M. C., Morse, J., et al. 2006, ApJ, 645, 283
Finkelstein, S. L., Morse, J. A., Green, J. C., et al. 2006, ApJ, 641, 919
García-Burillo, S., Graciá-Carpio, J., Guélin, M., et al. 2006, ApJ, 645, L17
Genzel, R., Lutz, D., Sturm, E., et al. 1998, ApJ, 498, 579
Gorjian, V., Cleary, K., Werner, M. W., & Lawrence, C. R. 2007, ApJ, 655, L73
Goulding, A. D., & Alexander, D. M. 2009, MNRAS, 398, 1165
Greenhill, L. J., Moran, J. M., & Herrnstein, J. R. 1997, ApJ, 481, L23
Guainazzi, M., Matt, G., Brandt, W. N., et al. 2000, A&A, 356, 463
Guélin, M., Salomé, P., Neri, R., et al. 2007, A&A, 462, L45
Higdon, S. J. U., Armus, L., Higdon, J. L., Soifer, B. T., & Spoon, H. W. W. 2006, ApJ, 648, 323
Ho, L. C., & Keto, E. 2007, ApJ, 658, 314
Houck, J. R., Roellig, T. L., van Cleve, J., et al. 2004, ApJS, 154, 18
Hurford, A. P., & Fesen, R. A. 1996, ApJ, 469, 246
Itoh, T., Done, C., Makishima, K., et al. 2008, PASJ, 60, 251
Iwasawa, K., Koyama, K., Awaki, H., et al. 1993, ApJ, 409, 155
Jura, M. 1974, ApJ, 190, L33
Jura, M., & York, D. G. 1978, ApJ, 219, 861
Karachentsev, I. D., Tully, R. B., Dolphin, A., et al. 2007, AJ, 133, 504
Lacy, J. H., Baas, F., Allamandola, L. J., et al. 1984, ApJ, 276, 533
Lenc, E., & Tingay, S. J. 2006, AJ, 132, 1333
Lenc, E., & Tingay, S. J. 2009, AJ, 137, 537
Lutz, D., Maiolino, R., Moorwood, A. F. M., et al. 2002, A&A, 396, 439
Madejski, G., Życki, P., Done, C., et al. 2000, ApJ, 535, L87
Marconi, A., Moorwood, A. F. M., Origlia, L., & Oliva, E. 1994, The Messenger, 78, 20
Marconi, A., Oliva, E., van der Werf, P. P., et al. 2000, A&A, 357, 24
Modica, F., Vavilkin, T., Evans, A. S., et al. 2010, AJ, submitted
Moorwood, A. F. M., & Oliva, E. 1988, A&A, 203, 278
Moorwood, A. F. M., & Oliva, E. 1994, ApJ, 429, 602
Moorwood, A. F. M., Lutz, D., Oliva, E., et al. 1996a, A&A, 315, L109
Moorwood, A. F. M., van der Werf, P. P., Kotilainen, J. K., Marconi, A., & Oliva, E. 1996b, A&A, 308, L1
Neufeld, D. A., Melnick, G. J., Sonnentrucker, P., et al. 2006, ApJ, 649, 816
Oliva, E., Salvati, M., Moorwood, A. F. M., & Marconi, A. 1994, A&A, 288, 457
Oliva, E., Moorwood, A. F. M., Drapatz, S., Lutz, D., & Sturm, E. 1999, A&A, 343, 943
Pedlar, A., Muxlow, T., & Wills, K. A. 2003, in Rev. Mex. Astron. Astrofis., 27, Rev. Mex. Astron. Astrofis. Conf. Ser., ed. J. Arthur, & W. J. Henney, 15, 303
Pereira-Santaella, M., Alonso-Herrero, A., Rieke, G. H., et al. 2010, ApJS, 188, 447
Pérez-Beaupuits, J. P., Aalto, S., & Gerebro, H. 2007, A&A, 476, 177
Pérez-Beaupuits, J. P., Spaans, M., van der Tak, F. F. S., et al. 2009, A&A, 503, 459
Pérez-Beaupuits, J. P., Spaans, M., Hogerheijde, M. R., et al. 2010, A&A, 510, A87
Prieto, M. A., Meisenheimer, K., Marco, O., et al. 2004, ApJ, 614, 135
Rice, W., Lonsdale, C. J., Soifer, B. T., et al. 1988, ApJS, 68, 91
Rieke, G. H., & Lebofsky, M. J. 1985, ApJ, 288, 618
Roche, P. F., & Aitken, D. K. 1984, MNRAS, 208, 481
Roussel, H., Helou, G., Smith, J. D., et al. 2006, ApJ, 646, 841
Roussel, H., Helou, G., Hollenbach, D. J., et al. 2007, ApJ, 669, 959
Smith, J. D. T., Armus, L., Dale, D. A., et al. 2007, PASP, 119, 1133
Smith, J. D. T., Rudnick, L., Delaney, T., et al. 2009, ApJ, 693, 713
Snijders, L., Kewley, L. J., & van der Werf, P. P. 2007, ApJ, 669, 269
Sonnentrucker, P., Friedman, S. D., Welty, D. E., York, D. G., & Snow, T. P. 2002, ApJ, 576, 241
Sonnentrucker, P., Friedman, S. D., Welty, D. E., York, D. G., & Snow, T. P. 2003, ApJ, 596, 350
Spoon, H. W. W., Koornneef, J., Moorwood, A. F. M., Lutz, D., & Tielens, A. G. G. M. 2000, A&A, 357, 898
Spoon, H. W. W., Moorwood, A. F. M., Pontoppidan, K. M., et al. 2003, A&A, 402, 499
Spoon, H. W. W., Marshall, J. A., Houck, J. R., et al. 2007, ApJ, 654, L49
Sturm, E., Lutz, D., Verma, A., et al. 2002, A&A, 393, 821
Thornley, M. D., Schreiber, N. M. F., Lutz, D., et al. 2000, ApJ, 539, 641
Tueller, J., Baumgartner, W. H., Markwardt, C. B., et al. 2010, ApJS, 186, 378
van der Werf, P. P., Isaak, K. G., Meijerink, R., et al. 2010, A&A, 518, L42
Veilleux, S., Rupke, D. S. N., Kim, D., et al. 2009, ApJS, 182, 628
Voit, G. M. 1992, ApJ, 399, 495
Weaver, K. A., Meléndez, M., Mushotzky, R. F., et al. 2010, ApJ, 716, 1151
Werner, M. W., Roellig, T. L., Low, F. J., et al. 2004, ApJS, 154, 1
Whittet, D. C. B. 2003, Dust in the galactic environment, ed. D. C. B. Whittet, Series in Astronomy and Astrophysics, ISBN 0750306246 (Bristol: Institute of Physics (IOP) Publishing)
Willett, K. W., Stocke, J. T., Darling, J., & Perlman, E. S. 2010, ApJ, 713, 1393